Manuscript Details

Manuscript number	VOLGEO_2019_182_R1
Title	An Examination of the Continuous Wavelet Transform for Volcano-Seismic Spectral Analysis
Article type	Research Paper

Abstract

Volcanoes produce widely varying seismic signals due to the presence of complex and non-linear physical processes. The temporal distribution of seismicity at volcanoes ranges from individual transients to swarms of many small events and protracted volcanic tremor. The spectral range of volcanic signals is unequivocally broadband, with coincident high (> 20 Hz) and very low (down to periods of hundreds of seconds) frequency signals frequently observed at many volcanic systems. As such, interpretations of volcano-seismic source and process require suitable characterisation in the time-frequency (T-F) domain. The adoption of automated approaches to routine seismic processing at volcanoes also creates the need to evaluate how we suitably extract discriminatory features of interest from such diverse volcano-seismic signals. Here we assess the performance of the continuous wavelet transform (CWT) for spectral representations of volcano-seismic signals. The localisation property of wavelet transforms gives the CWT a distinct advantage over commonly used moving-window Fourier transforms, enabling it to capture sharp changes in signal and represent signals over a wide range of timescales. Examination of seismic data for typical volcano-seismic phenomena, such as volcano-tectonic earthquakes (VTs), shows that CWT scalograms have better T-F resolution across broader frequency ranges than Fourier transform spectrograms, which suffer from greater spectral smearing in the time domain at higher frequencies. The inherent log-scale representation of CWT scalograms is also better suited for detection and representation of very-long-period (VLP) signals and for distinguishing volcanic signals from ambient microseismic noise. When applied to seismic data from Santiaguito volcano in Guatemala, CWT analysis reveals pre- and syn-eruptive signals across a wide range of frequency bands, ranging from 600 s to 50 Hz, with ultra-long-period signals (ULPs; 30 to 600 s) detected on instruments up to 1.9 km from the active vent, which is beyond the range of previously detected ULPs at this volcanic system. The CWT scalogram conveniently represents these simultaneous syn-eruptive spectral features in a single plot, which can aid exploratory analysis and inform source models. Furthermore, the ‘edge detection’ capabilities of the CWT accurately identify sharp changes in the raw signal over the VLP-ULP frequency range (5 to 600+ s), thought to represent sudden deflation associated with eruption, providing a useful tool for ‘picking’ explosive eruptions. The addition of an average wavelet energy distribution to CWT scalograms, which reveals the average energy across the whole signal at each wavelet scale, is also useful for characterising spectral content and identifying spectral peaks, as its smooth appearance is easier to interpret than FFT spectral amplitude plots. We conclude that wavelet transform methods are underutilised in volcano seismology, where their T-F localisation properties would be particularly well-suited, and suggest potential applications in terms of automated event detection and classification.

Keywords	wavelet transform; volcano seismology; explosion seismicity; ULP; low-oscillation wavelet

Corresponding Author	Sacha Lapins
Corresponding Author's Institution	University of Bristol
Order of Authors	Sacha Lapins, Diana Roman, Jonathan Rougier, Silvio De Angelis, Katharine Cashman, Michael Kendall
Suggested reviewers	Greg Waite, Seth Moran, Weston Thelen, Jeffrey Johnson

Title: An Examination of the Continuous Wavelet Transform for Volcano-Seismic Spectral Analysis

Authors: Sacha Lapins[1], Diana C. Roman[2], Jonathan Rougier[3], Silvio De Angelis[4], Katharine V. Cashman[1], J.-Michael Kendall[1]

[1]School of Earth Sciences, University of Bristol
[2]Department of Terrestrial Magnetism, Carnegie Institution of Washington
[3]School of Mathematics, University of Bristol
[4]School of Environmental Sciences, University of Liverpool

ABSTRACT

Volcanoes produce widely varying seismic signals due to the presence of complex and non-linear physical processes. The temporal distribution of seismicity at volcanoes ranges from individual transients to swarms of many small events and protracted volcanic tremor. The spectral range of volcanic signals is unequivocally broadband, with coincident high (> 20 Hz) and very low (down to periods of hundreds of seconds) frequency signals frequently observed at many volcanic systems. As such, interpretations of volcano-seismic source and process require suitable characterisation in the time-frequency (T-F) domain. The adoption of automated approaches to routine seismic processing at volcanoes also creates the need to evaluate how we suitably extract discriminatory features of interest from such diverse volcano-seismic signals.

Here we assess the performance of the continuous wavelet transform (CWT) for spectral representations of volcano-seismic signals. The localisation property of wavelet transforms gives the CWT a distinct advantage over commonly used moving-window Fourier transforms, enabling it to capture sharp changes in signal and represent signals over a wide range of timescales. Examination of seismic data for typical volcano-seismic phenomena, such as volcano-tectonic earthquakes (VTs), shows that CWT scalograms have better T-F resolution across broader frequency ranges than Fourier transform spectrograms, which suffer from greater spectral smearing in the time domain at higher frequencies. The inherent log-scale representation of CWT scalograms is also better suited for detection and representation of very-long-period (VLP) signals and for distinguishing volcanic signals from ambient microseismic noise.

When applied to seismic data from Santiaguito volcano in Guatemala, CWT analysis reveals pre- and syn-eruptive signals across a wide range of frequency bands, ranging from 600 s to 50 Hz, with ultra-long-period signals (ULPs; 30 to 600 s) detected on instruments up to 1.9 km from the active vent, which is beyond the range of previously detected ULPs at this volcanic system. The CWT scalogram conveniently represents these simultaneous syn-eruptive spectral features in a single plot, which can aid exploratory analysis and inform source models. Furthermore, the ‘edge detection’ capabilities of the CWT accurately identify sharp changes in the raw signal over the VLP-ULP frequency range (5 to 600+ s), thought to represent sudden deflation associated with eruption, providing a useful tool for ‘picking’ explosive eruptions.

The addition of an average wavelet energy distribution to CWT scalograms, which reveals the average energy across the whole signal at each wavelet scale, is also useful for characterising spectral content and identifying spectral peaks, as its smooth appearance is easier to interpret than FFT spectral amplitude plots.

We conclude that wavelet transform methods are underutilised in volcano seismology, where their T-F localisation properties would be particularly well-suited, and suggest potential applications in terms of automated event detection and classification.

1 INTRODUCTION

Spectral analysis forms a key part of interpreting volcano-seismic signals. Eruptions are almost always preceded by changes in seismicity (McNutt and Roman, 2015) – understanding and characterising patterns of seismicity can therefore reveal important information regarding the likelihood, timing and severity of eruption (e.g., Chouet and Matoza, 2013; McCausland et al., 2017; McNutt, 1996; Phillipson et al., 2013; Power et al., 1992). The complex nature and high occurrence rates of pre- and syn-eruptive seismicity make manual analysis of volcanic-seismic events extremely time-consuming and has stimulated development and deployment of automated approaches to detect and classify volcano-seismic events (e.g., Maggi et al., 2017; Soubestre et al., 2018). Such methods, however, often require suitable extraction of signal features of interest in order to adequately identify a diverse range of volcanic event types. Localising subtle changes in frequency content through time also provides information on the shallow dynamics of a volcanic system (e.g., Johnson et al., 2018) and can help constrain inversions for source parameters. Thus, the need arises to evaluate the most meaningful way to characterise the time-varying spectral content of volcano-seismic signals and how it relates to source mechanism and eruption likelihood.

Signals are generally transformed into the 1-D spectral domain through implementation of Fourier transforms, in particular the fast Fourier transform algorithm (FFT; Cooley and Tukey, 1965). However, as seismic event classification at volcanoes is based on both frequency- and time-dependent characteristics of a signal (e.g., impulsive vs. emergent, duration of dominant frequencies, coda length, rate of occurrence), a spectral decomposition in 2-D time-frequency (T-F) space is typically required. In practice, this is usually achieved using sliding window Fourier techniques, such as the short-time Fourier transform (STFT), which calculate the Fourier transform over smaller, overlapping, finite-length time windows. However, these techniques require segmentation of the signal into windows of fixed length, and thus suffer from a T-F resolution trade-off: short windows provide relatively good time resolution but at the cost of poorer frequency resolution and truncate the overall determinable spectral range; conversely, long time windows more accurately determine the spectral components of a signal and extend the determinable spectral range but changes in the time domain are averaged across the long window length, leading to ‘smearing’ (Addison, 2016; Chakraborty and Okaya, 1995; Tary et al., 2014). This is particularly problematic with volcano-seismic signals, where the useful spectral range is vast, ranging from high frequency features of interest (up to 15 Hz;

Lahr et al., 1994) to so-called very- and ultra-long period features (< 0.01 Hz or, equivalently, > 100 s period; Aster et al., 2008; Chouet et al., 2005; D'Auria et al., 2006; Genco and Ripepe, 2010; Kawakatsu et al., 2000; Sanderson et al., 2010). Furthermore, the infinite (or non-localised) reach of the sine and cosine functions that make up the basis of standard Fourier transforms are ill-equipped to handle sharp changes and transient features, resulting in insufficient T-F localisation of event onsets, phase arrivals or other signal features of interest and the generation of spurious harmonics (Bowman and Lees, 2013).

To be of most use, spectral estimation techniques for volcano-seismic studies must therefore be adaptable to broadband frequency scales, with basis functions that match varying signal criteria (i.e., not just sines and cosines) and that are well-localised in both the time and frequency domains. These requirements are well met by wavelet transforms, which employ basis functions that are localised in both time and frequency space, providing sparser representations and better T-F resolution across a wide range of timescales.

In this study we critically assess the suitability of the continuous wavelet transform (CWT) for spectral representations of volcano-seismic signals and present guidelines for its use in routine processing. Those familiar with the concepts of Fourier and wavelet transforms can skip Section 2, which provides a brief conceptual background. The subsequent sections compare the Fourier transform and CWT for the analysis of 'typical' volcano-seismic signals previously presented by McNutt and Roman (2015) and apply the CWT to a case study from the continuously active Santiaguito volcanic dome complex in Guatemala, where wide ranging spectral signals have previously been identified (e.g., Johnson et al., 2014; Sanderson et al., 2010). The paper concludes with a discussion of utility, performance and further potential applications in Section 5 and conclusions in Section 6.

2. BACKGROUND

In this section, we provide a brief conceptual background on Fourier and wavelet transforms, along with a description of the Morlet wavelet used in our analyses.

2.1 FOURIER TRANSFORM

The wavelet transform is strongly linked to the Fourier transform, in that both are derived from the inner product of a signal, $x(t)$, with a template function, $\psi(t)$:

$$\langle x(t),\psi(t)\rangle = \int x(t)\psi^*(t)dt, \tag{2.1}$$

where $\psi^*(t)$ is the complex conjugate of $\psi(t)$. This inner product operator essentially measures the similarity between the signal, $x(t)$, and the template function, $\psi(t)$. In the case of the Fourier transform, this template function is the complex sine and cosine function, $e^{i\omega t}$:

$$F(\omega) = \langle x(t),e^{i\omega t}\rangle = \int_{-\infty}^{\infty} x(t)e^{-i\omega t}dt, \tag{2.2}$$

where F is the Fourier transform of signal x, ω is angular frequency related to Hertz frequency f by the relationship $\omega = 2\pi f$, t is time, and $e^{i\omega t} = \cos(\omega t) + i\sin(\omega t)$ by Euler's formula. The Fourier transform is applied to the whole signal and therefore assumes stationarity – it will not provide information regarding local concentrations of energy in the time domain. As such, the Fourier transform is generally implemented over successive, fixed-length, overlapping windows of the signal to examine time-varying spectral content through STFT spectrograms. The STFT at time instant b and angular frequency ω is defined as:

$$S(\tau,\omega) = \int_{-\infty}^{\infty} x(t)w(t-b)e^{-i\omega t}dt, \tag{2.3}$$

where $x(t)$ is the signal, $w(t-b)$ is the window function, usually a Hann or Gaussian window in practice (Tary et al., 2014), and $e^{-i\omega t}$ is the Fourier kernel. Most common seismic

processing codes (e.g., SAC; Goldstein and Snoke, 2005) use Fourier transforms as the basis for spectral representations of seismic waveforms.

2.2 WAVELET TRANSFORM

The wavelet transform is hardly a novel technique in geophysics. Essentially a measure of similarity between a localised wavelet function and a signal, wavelet transform analysis as we know it was initially developed for seismic signal analysis in the 1980s (e.g., Goupillaud et al., 1984; Grossmann and Morlet, 1984; Morlet et al., 1982b, 1982a) and underwent great research and development in the fields of mathematics and engineering during the 1990s (e.g., Daubechies, 1992), before gaining popularity with applications throughout the sciences. While the wavelet transform is commonly utilised in 'conventional' tectonic and exploration seismology, its use in volcanology has been less prevalent. Recently, however, wavelet transform methods have seen a rise in popularity in volcanological studies: e.g., for analysis of volcano-seismic event cyclicity (Odbert et al., 2014; Vargas-Bracamontes et al., 2009); cross-correlation between seismicity and infrasound or gas emissions (Cannata et al., 2013; Conde et al., 2016); source localisation in self-potential surveys (Saracco et al., 2004); coherence between seismic velocity changes and air temperature (Cannata et al., 2017); and peri-volcanic surface deformation (Shirzaei, 2013). It appears, however, that application of the wavelet transform to broadband volcano-seismic spectral analysis, where it is particularly well-suited due to signal non-stationarity, transient feature localisation and the wide-varying frequency scales of interest, is still limited to only a small number of studies (e.g., Bartosch and Seidl, 1999; Lees and Ruiz, 2008).

In much the same way as the Fourier transform, the wavelet transform is the measure of similarity between a signal and a template function, $\psi(t)$, known as the *mother wavelet*, at varying scales and locations. The key difference is that the template function in the wavelet transform does not require windowing of the signal, is fast-decaying towards zero (and therefore localised), and is not restricted to possessing smooth periodic characteristics, such as the sine or cosine function, allowing for better localised matching of the wavelet and signal. It should be noted that, despite these localisation properties, the wavelet transform is still subject to a T-F resolution trade-off that relates to the effective 'window length' at a given scale of the wavelet used (see *Heisenberg boxes* in e.g., Addison, 2016; Mallat, 2009).

The template function, $\psi(t)$, must satisfy certain mathematical conditions in order to be a wavelet. These are:

1. It must "decay" to zero at $\pm\infty$ (i.e., have *finite energy*):

$$E = \int_{-\infty}^{\infty} |\psi(t)|^2 dt < \infty, \tag{2.4}$$

where E denotes energy and $|\psi(t)|^2$ is the square of the magnitude of $\psi(t)$. This condition ensures that the mother wavelet is localised. The space of functions that satisfy this mathematical condition is denoted $L^2(\mathbb{R})$.

2. It must have *zero mean*:

$$\int_{-\infty}^{\infty} \psi(t) dt = 0. \tag{2.5}$$

More precisely, if $\hat{\psi}(\omega)$ is the Fourier transform of $\psi(t)$, i.e.,

$$\hat{\psi}(\omega) = \int_{-\infty}^{\infty} \psi(t) e^{-i\omega t} dt, \tag{2.6}$$

then the following *admissibility condition* must hold:

$$C_g = \int_{-\infty}^{\infty} \frac{|\hat{\psi}(\omega)|^2}{\omega} d\omega < \infty, \tag{2.7}$$

which implies that the wavelet has zero mean and no zero-frequency component, i.e., $\hat{\psi}(0) = 0$. C_g is known as the *admissibility constant* and is used to recover the total energy in the signal or reconstruct the original signal through the inverse wavelet transform (Addison, 2016).

To compute the CWT, we can denote the mother wavelet, $\psi(t)$, in terms of dilation (or scale) parameter, a, and translation (or location) parameter, b, such that

$$\psi_{a,b}(t) = \psi\left(\frac{t-b}{a}\right). \tag{2.8}$$

The original mother wavelet is given by $a = 1$ and $b = 0$. We can then scale and shift the mother wavelet by changing a and b, without the need for windowing the signal.

The *continuous wavelet transform* of a signal, $x(t)$, with respect to the mother wavelet, $\psi_{a,b}(t)$, is then defined as:

$$T(a,b) = \langle x(t), \psi_{a,b}(t) \rangle = \int_{-\infty}^{\infty} x(t)\psi^*\left(\frac{t-b}{a}\right)dt, \tag{2.9}$$

where $T(a,b)$ denotes the CWT at scale a and location b. When the wavelet correlates well with the signal at scale a and location b, we get a large magnitude of $|T(a,b)|$. Typically, when performing spectral analysis, one is interested in the energy (or power) of the signal, $E(a,b) = |T(a,b)|^2$. A plot of $E(a,b)$ is sometimes known as a *scalogram* (Fig. 1), the CWT equivalent of a Fourier transform spectrogram.

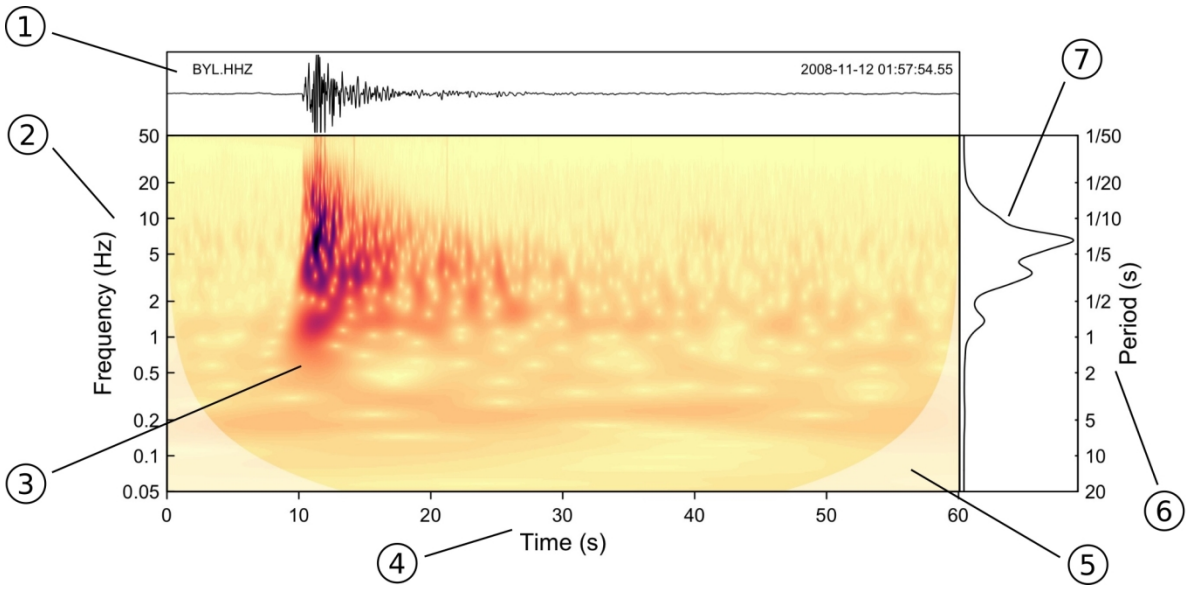

Figure 1 – Example of CWT scalogram. *1) Raw signal with station name, instrument component and time stamp; 2) Left vertical axis is frequency in Hertz (scaled logarithmically); 3) Main 'scalogram' yielding T-F estimation of signal (dark values are higher energy, light values are lower energy); 4) Horizontal time axis in seconds; 5) Potential edge effect at each*

wavelet scale ('cone of influence'); 6) Right vertical axis is period in seconds; 7) Average wavelet energy distribution (average energy across all time points at each wavelet scale).

In practice, analysis of discretely sampled physical processes, with a given sample rate δt, requires an approximation using the *discretised* CWT (e.g., Torrence and Compo, 1998):

$$T(a,b) = \sum_{t=1}^{N} x_t \psi^* \left[\frac{(t-b)\delta t}{a}\right]. \quad (2.10)$$

In its discretised form, convolution of the signal and wavelet function must be performed N times (where $b \in t = 1, ..., N$, the number of time points in the signal) at each wavelet scale, a, which can become very computationally expensive. The convolution theorem allows us to perform these product calculations at all time locations b simultaneously for a given wavelet scale, a, and sample rate, δt, through the more efficient inverse Fourier transform of the product:

$$T(a,b) = \sum_{k=0}^{M-1} \hat{x}_k \hat{\psi}^* (a\omega_k) e^{i\omega_k b \delta t}, \quad (2.11)$$

(e.g., Meyers et al., 1993; Torrence and Compo, 1998) where $k = 0, ..., M-1$ is the frequency index with $M = N$, the number of samples in the signal, and $\hat{x}$ and $\hat{\psi}$ represent the Fourier transform of the signal, x, and wavelet template function, ψ, respectively. The angular frequency ω_k for each k is defined as

$$\omega_k = \begin{cases} \frac{2\pi k}{M\delta t}, & k \leq \frac{M}{2} \\ -\frac{2\pi k}{M\delta t}, & k > \frac{M}{2} \end{cases}, \quad (2.12)$$

and effectively re-scales the wavelet to accommodate a given sample rate, δt, returning the output in terms of chosen wavelet scale, a.

There also exists a discrete wavelet transform (DWT), which can provide orthonormal transforms of the original signal, allowing complete and efficient reconstruction of the signal without redundancy. However, wavelets in the DWT are always scaled by integer powers of 2 (i.e., the scale parameter is 2^j, $j = 1, 2, 3, ...$), providing coarser representations in both the frequency and time domains. The CWT is preferred for this study due to its over-completeness – the wavelet scales and time-shifts can be subdivided so that the wavelet transform can be conducted 'continuously' over the entire set of wavelet scales and time steps, providing finer frequency and time resolution but at the cost of overlap and correlation between wavelet (sub)scales and time-shifts.

2.3 MORLET WAVELET

The choice of wavelets is vast (theoretically infinite; Aguiar-Conraria and Soares, 2011) and completely dependent on the application (e.g., Schukin et al., 2004). A commonly used complex wavelet in CWT analysis is the Morlet wavelet, which is used throughout this study as its periodic sinusoidal form means that wavelet scales can very reasonably be approximated in terms of Hz frequency and interpretation can therefore be linked to the existing vast body of work in volcano-seismology based on Fourier frequencies. It is defined as:

$$\psi_{\omega_0}(t) = \pi^{-1/4}(e^{i\omega_0 t} - e^{-{\omega_0}^2/2})e^{-t^2/2}, \tag{2.13}$$

where ω_0 is the Morlet wavelet's 'central frequency' that effectively controls the trade-off between time and frequency resolutions (Fig. 3 bottom), $e^{i\omega_0 t}$ is the complex sinusoid $\cos(\omega_0 t) + i\sin(\omega_0 t)$, $e^{-t^2/2}$ is a Gaussian window, $e^{-{\omega_0}^2/2}$ is the correction for non-zero mean (negligible for $\omega_0 \geq 5$) and $\pi^{-1/4}$ is a normalisation constant.

Conceptually, the Morlet wavelet is similar to the STFT in that it is a (complex) sine wave within a Gaussian window (Fig. 3 bottom). However, unlike the fixed-length window of the STFT, where the internal frequency must vary, the 'window length' of the Morlet wavelet changes with wavelet scale so that the number of oscillations within the window remains the same. The Morlet wavelet's complex nature, where the real and imaginary parts differ in phase by a quarter period, is desirable over real-valued wavelets as it also allows phase information from the signal to be extracted, providing scope to conduct analysis of polarisation attributes and complex filtering steps in the wavelet domain (e.g., Kulesh et al., 2007).

The Morlet wavelet can also reasonably be approximated in terms of Fourier frequency, unlike highly irregular and aperiodic wavelets, where such an approximation can be effectively meaningless or, even worse, misleading (Meyers et al., 1993). Its simple structure also prevents additional components or artefacts being generated in wavelet space, as opposed to when using more complex wavelets (Addison, 2018). The mother wavelet, i.e., the wavelet at scale $a = 1$, is generally assigned a characteristic frequency, f_c, and the Fourier frequency, f, for a given wavelet scale, a, approximated by the linear relationship

$$f = \frac{f_c}{a} \tag{2.14}$$

This characteristic frequency may be the spectral peak (Meyers et al., 1993; Torrence and Compo, 1998) or passband centre (Addison, 2016) of the wavelet's energy spectrum, or the wavelet's central frequency, ω_0, expressed in Hz frequency $f_0 = \omega_0/2\pi$. Throughout this study, we use the latter ($f_c = f_0$) to relate wavelet scale to Fourier frequency.

3 APPLICATION OF CWT TO TYPICAL VOLCANO-SEISMIC SIGNALS

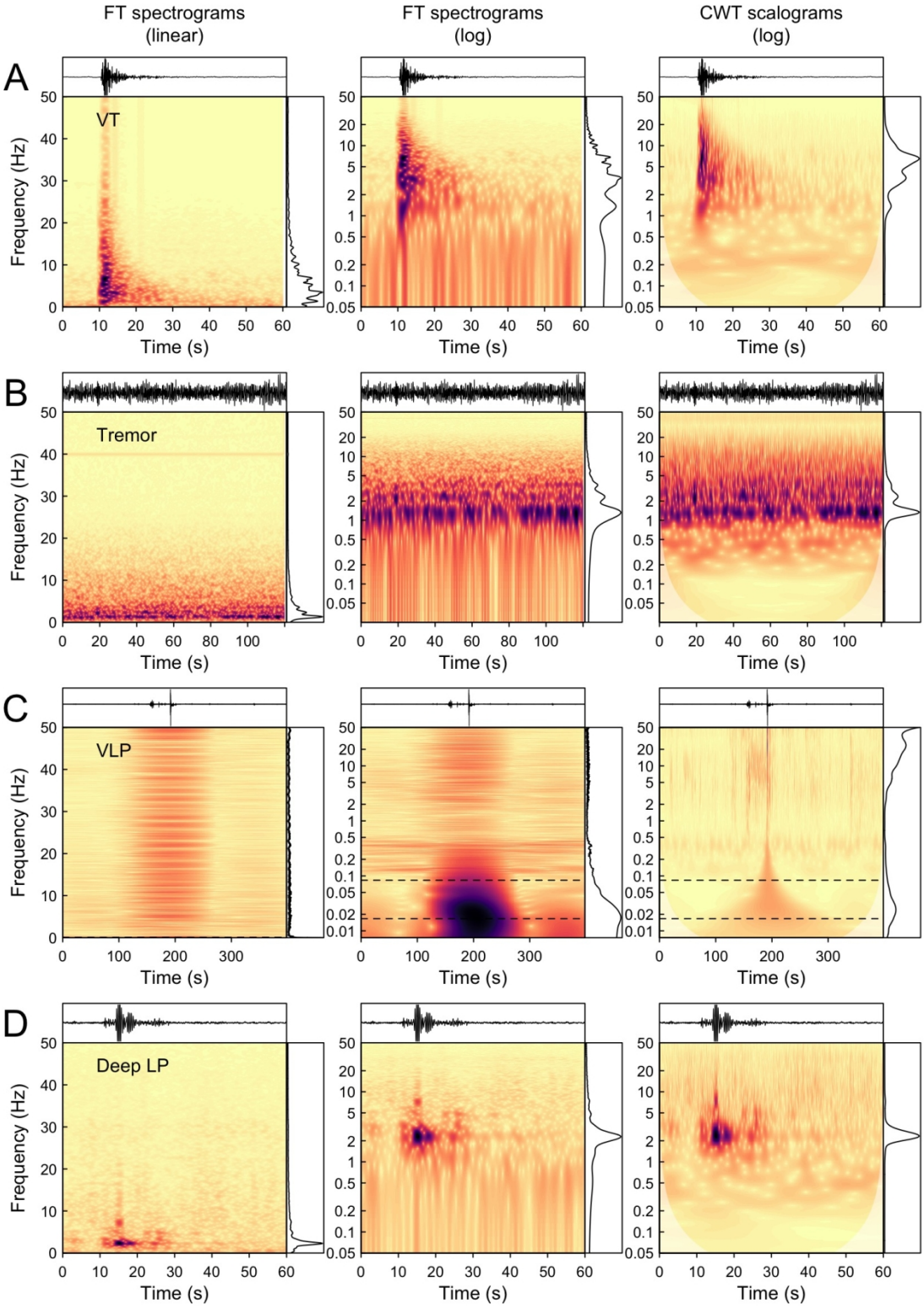

Figure 2 – Linear-scaled STFT spectrograms *(left)*, ***log-scaled STFT spectrograms*** *(middle)* ***and CWT scalograms*** *(right)* ***for typical volcano-seismic events published in McNutt & Roman (2015) (part one).*** *A) VT earthquake recorded at Kilauea volcano, Hawaii; B) Volcanic tremor recorded at Kilauea volcano, Hawaii; C) VLP event recorded at Fuego volcano, Guatemala (horizontal dashed lines are 12 s and 60 s period bounds); D) Deep LP event recorded at Akutan volcano, Alaska. All STFT spectrograms were produced using 3 s Hann window with 99 % overlap, except the VLP event in C) which was produced using a 180 s Hann window and 99 % overlap. All CWT scalograms were produced using Morlet wavelet with central frequency* $\omega_0 = 6$.

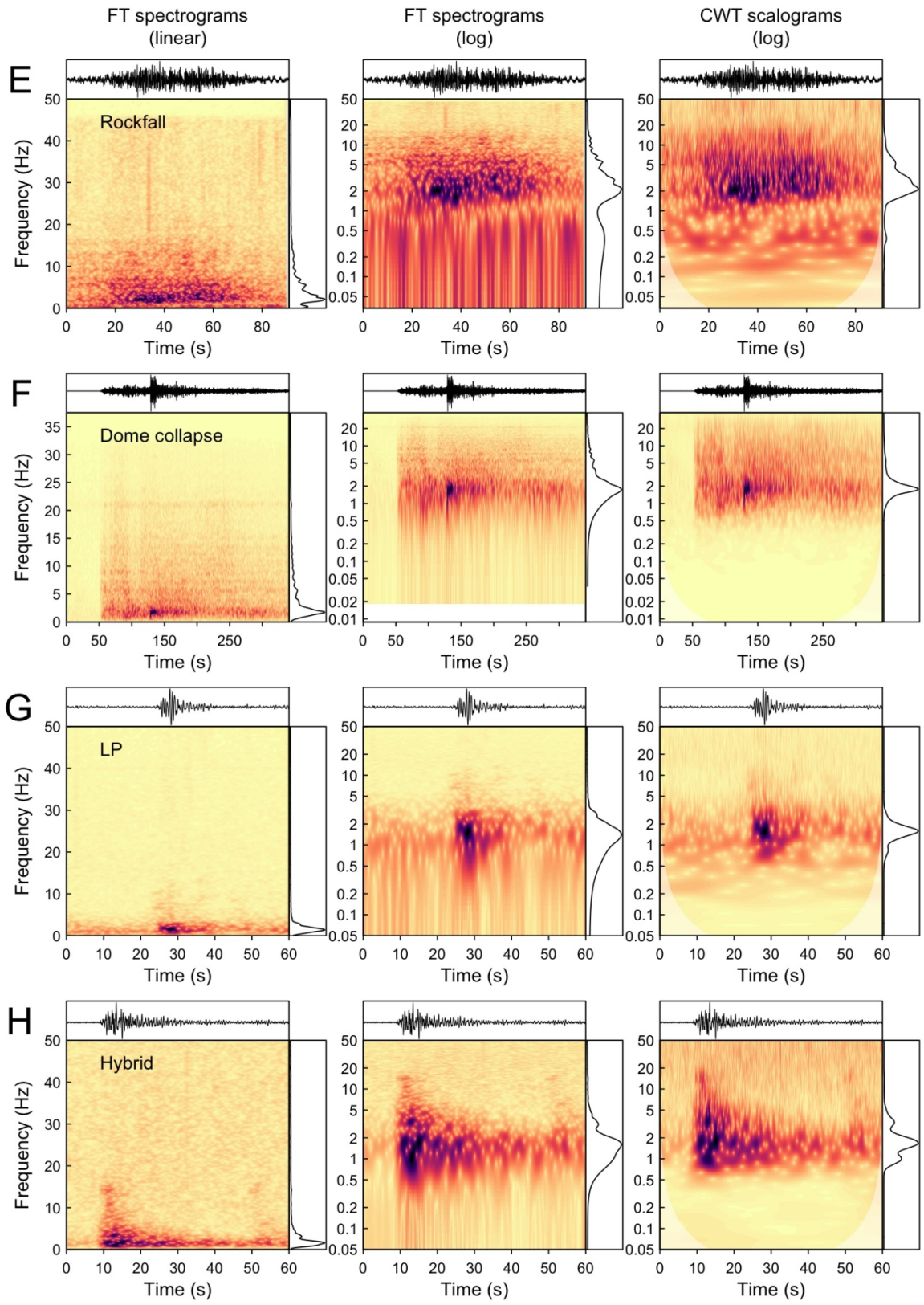

287

Figure 2 (cont.) – Linear-scaled STFT spectrograms *(left)*, ***log-scaled STFT spectrograms*** *(middle)* ***and CWT scalograms*** *(right)* ***for typical volcano-seismic events published in McNutt & Roman (2015) (part two)****. E) Rockfall event recorded at Soufrière Hills volcano, Montserrat; F) Dome collapse + explosion recorded at Soufrière Hills volcano, Montserrat; G) LP event recorded at Shishaldin volcano, Alaska; H) Hybrid event recorded at Mt. St. Helens volcano, Washington. All STFT spectrograms were produced using 3 s Hann window with 99 % overlap. All CWT scalograms were produced using Morlet wavelet with central frequency* $\omega_0 = 6$.

288

To assess the performance of CWT scalograms for characterisation of various volcano-seismic events, and for direct comparison with Fourier transform spectrogram plots, we analysed a dataset comprising vertical-component seismic data for typical volcano-seismic phenomena, such as volcano-tectonic events (VTs), very-long-period signals (VLPs), tremor and rockfalls (Fig. 2). This dataset was originally compiled by McNutt and Roman (2015); all analyses and plots were produced in R (R Core Team, 2017). Throughout this study we use a square-root amplitude scale for STFT spectrograms and a fourth-root amplitude scale for CWT scalograms, except when using solely the imaginary part of the Morlet wavelet in Figures 7, 10 and 11, where no amplitide scaling is applied. These yield similar relative power of features across the respective spectra for each method and perform well in the visual representation of broadband signals over many orders of scale and magnitude. All plots are self-normalised and references to linear- and log-scaling throughout this study relate to frequency axes, as opposed to amplitude scaling.

All seismograms in the original publication by McNutt and Roman (2015) were bandpass filtered between 0.1 and 10 Hz, with the exception of the Fuego VLP (Fig. 2C), which was bandpass filtered between 60 and 12 s periods and downsampled from 200 Hz to 25 Hz. Conversely, in this study, all signals have been left in their raw, original form to facilitate direct comparison of the inherent linear scale of Fourier spectrogram with the CWT's inherent log scale for feature determination across wide ranging frequency scales. Conducting a wavelet transform between predetermined upper and lower frequency bounds is also essentially a bandpass filtering process in its own right so prior filtering is not required. The only pre-processing step, therefore, was to subtract the signal mean to reduce the influence of edge effects on the subsequent spectrograms and scalograms. Although the localisation property of the CWT means these edge effects generally manifest at the beginning and end of the signal, large edge effects can diminish the comparative strength of features of interest. Similarly, edge effects can propogate throughout the whole signal in STFT spectrograms and contaminate large parts of the spectrum so mean and trend removal is equally necessary. The upper and lower frequency limits in the log-scale STFT spectrograms and CWT scalograms have been chosen as the instrument Nyquist and $3 / t$ Hz (t = total signal length in seconds), respectively.

A stand-out example from the comparative spectral analyses is the VLP event from Fuego volcano, Guatemala (Fig. 2C). VLP signals have a spectral period of tens of seconds and range from single 'spikes' or bell-shaped 'bumps' to longer irregularly-shaped (i.e., non-sinusoidal)

waveforms over several minutes (e.g., Chouet et al., 2008; Chouet and Matoza, 2013; Hill et al., 2002; Waite et al., 2013). They exhibit strong self-similarity, suggesting a stable, non-destructive source (Chouet et al., 2010; Lyons and Waite, 2011; Waite et al., 2013). Good characterisation of these signals therefore provides an opportunity to examine eruption dynamics and exploit this self-similarity from an event detection point of view. Figure 2C shows (from left to right) linear- and log-scaled STFT spectrograms and a CWT scalogram for a vertical component trace containing a VLP event with dominant energy between 12 s and 60 s period (0.0833 Hz and 0.0167 Hz respectively), as published by McNutt and Roman (2015). The horizontal dashed lines in Figure 2C indicate these upper and lower bounds. A window length of 180 s was used in the STFT to fully encompass signals down to 60 s period.

First, of note, the use of such a long window has caused extensive horizontal smearing in the time domain of both the linear- and log-scaled STFT spectrograms (Fig. 2C, left and middle), rendering the higher frequency bursts of energy completely indistinguishable from one another. Characterising the higher frequency content using a shorter window, however, would fail to encompass and characterise the VLP energy at all. The linear representation of the STFT spectrogram (Fig. 2C, left) is also ill-suited to visualise such long-period signals, regardless of STFT window length used. The horizontal dashed lines at 12 s and 60 s periods are not visible in the linear-scaled STFT spectrogram due to their extremely low frequency values. Linear-scaled spectrograms cannot, therefore, be used to ascertain the presence or absence of VLP signals. The log-scaled representation of the STFT spectrogram shows a pronounced feature (dark ‘blob’ in Fig. 2C, middle) below 0.05 Hz (20 s period). The relative weight of this VLP feature is far greater than the signal above 1 Hz and appears to have been greatly exaggerated: such a strong spectral feature should dominate the raw signal, which is not the case. Furthermore, the lower frequency bound of this VLP feature is not well constrained, with strong energy continuing below 0.01 Hz (100 s period), and there is strong horizontal smearing around the event due to the long window length used.

The CWT scalogram, in contrast, provides comparatively good characterisation across the whole spectrum, with the visible bursts of higher frequency energy in the raw signal delineated very clearly in the higher frequency range (> 1 Hz), and the VLP signal well characterised and constrained in the lower frequency range (< 0.2 Hz). The VLP signal manifests as a distincitive funnel shape in the CWT scalogram: this is characteristic of the analytic wavelet encountering a sharp discontinuity in the signal and is a result of the widening ‘window length’ as wavelet

scale increases (Addison, 2016). This reveals that the analytic wavelet encounters a sudden, marked change in ground velocity within the VLP range, rather than a smooth transition. The distribution of energy plot on the right-hand side of the CWT scalogram shows that energy remains strong down to around 0.02 Hz (50 s period) before tapering off. CWT scalograms are known for yielding excellent frequency resolution at very low frequencies, at the cost of reduced temporal resolution. Thus, it is unsurprising that energy is better constrained in the frequency domain of the CWT scalogram than in the STFT spectrograms at these very long periods. The downside to this high frequency resolution is that it can be hard to distinguish onset/duration, although that is no easier with the STFT spectrogram due to smearing from the long window length used. The use of a Morlet wavelet with lower central frequency (e.g., $\omega_0 = 1$) can greatly improve temporal resolution, but at the cost of greatly reduced frequency resolution (Fig. 3, left; Addison et al., 2002). Conversely, frequency resolution can be improved further, with even poorer temporal resolution, through use of a higher central frequency (e.g., $\omega_0 = 12$; Fig. 3, right). The central frequency parameter ω_0 therefore effectively controls the width of the wavelet at a given scale and the trade-off between time and frequency resolution, with values of ω_0 between 5 and 6 being most commonly employed (Addison, 2016).

The strength of this VLP feature, relative to the higher frequency content, in the CWT scalogram in Figure 2C (right) also appears more appropriate than in the corresponding log-scaled STFT spectrogram, with the average energy being roughly equal to that of the 5-20 Hz range. It should be noted that the CWT's inherent bias towards longer period components (Liu et al., 2007) has been removed in all scalograms in this study. The strongest energy in this range (i.e., the 'darkest' region in the lower half of the CWT scalogram) appears to be between 0.2 and 0.02 Hz (5 and 50 s period, respectively), which is consistent with the range given by McNutt and Roman (2015; horizontal dashed lines).

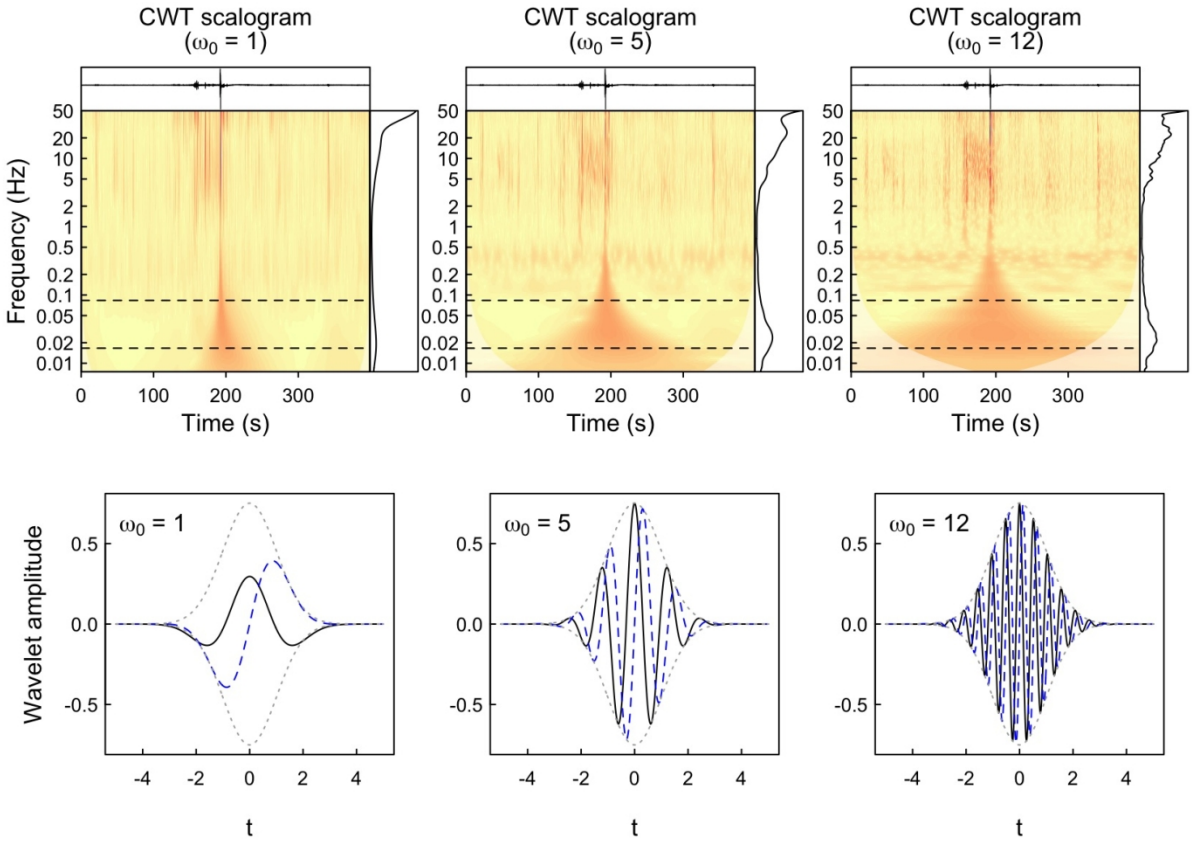

Figure 3 – Top: Comparison of CWT scalograms for VLP event using Morlet wavelet with differing central frequencies *(left: $\omega_0 = 1$, middle: $\omega_0 = 5$, right: $\omega_0 = 12$).* ***Bottom: Corresponding Morlet wavelets at scale a = 1*** *(solid black line = real part of Morlet wavelet; dashed blue line = imaginary part of Morlet wavelet; dotted grey line = Morlet wavelet's Gaussian window). Frequency resolution in scalograms (top) improves from left to right, at the cost of reduced time resolution. Conversely, time resolution improves from right to left, at the cost of reduced frequency resolution.*

There are also noticeable characteristic differences between the CWT and STFT approaches for the other examples of volcano-seismic phenomena in Figure 2; for example, the VT event from Kilauea volcano in Figure 2A. VTs are analogous to conventional tectonic earthquakes, in that they are thought to result from abrupt shear-failure or slip, with double-couple source mechanisms (Chouet and Matoza, 2013), and have dominant energy across 1.5 – 15 Hz (Lahr et al., 1994). They often occur in swarms (e.g., White and McCausland, 2016) and reflect shallow subsurface magma intrusion (e.g., Lu et al., 2000; Moran et al., 2011; Roman and Power, 2011) that in some cases proceeds to eruption (Power et al., 1992; Roman et al., 2006, 2004). The excellent time resolution of wavelet transforms at higher frequencies makes them conceptually well-suited for characterisation of VT onset times and durations. As such, T-F characterisation, polarisation attributes (e.g., Kulesh et al., 2007) and onset time determination (e.g., Bogiatzis and Ishii, 2015) through CWT analysis could aid both manual and automated classification (e.g., Bicego et al., 2013; Curilem et al., 2016; Hibert et al., 2017; Maggi et al., 2017) and provide useful clues regarding eruption likelihood.

Time resolution in the CWT scalogram (Fig. 2A, right) is indeed generally very good, at least above 2 Hz, where the effective 'width' of the analytic wavelet becomes shorter than the STFT window used (based on a 99.8% 'confidence interval' of the wavelet's Gaussian window with standard deviation $\sigma =$ a, the corresponding wavelet scale at a given frequency). Conversely, the STFT spectrograms show consistent horizontal smearing in the time domain (Fig. 2A, left and middle) as a result of windowing the signal. The improved time resolution at higher frequencies in the CWT scalogram does come at the cost of poorer frequency resolution (vertical smearing), although the dominant frequency components at approximately 1.4, 3.4 and 6.5 Hz are still well delineated, consistent with multi-frequency components that often characterise VTs (e.g., Hibert et al., 2011; Tary et al., 2014). These are perhaps easier to discern in the energy distribution plots of the CWT approach than in the corresponding energy distribution plots to the right-hand side of the linear- and log-scaled STFT spectrograms (Fig. 2A, left and middle). To achieve acceptable temporal resolution in the STFT spectrograms, the lower frequency range of the VT (i.e., < 1 Hz) is either poorly constrained (log-scaled) or impossible to discern (linear-scaled). Although, in this case, there is little of interest below 1 Hz, this lack of information could impact on manual or automated classification of such events, especially when event type is unknown a priori.

Further evidence of the utility of the CWT can be seen in Figures 2G & H, which show a long-period (LP) event from Shishaldin volcano and 'hybrid' event from Mount St Helens, respectively. Both events are characterised by lower frequency content than VTs (e.g., Bean et al., 2013; Chouet and Matoza, 2013; Lahr et al., 1994; Fig. 2). This is poorly constrained in the log-scaled STFT spectrograms, which show strong vertical smearing below 1 Hz, and is not visible in the corresponding linear-scaled STFT spectrograms. The CWT scalograms, in contrast, detect spectral peaks around and below 1 Hz, aptly characterise the lower frequency bounds and still retain high time resolution at higher frequencies, and are thus suitable for both diverse event classification and onset determination. Similar low frequency characterisation can be seen with the Kilauea tremor signal in Figure 2B, where the spectral peak between 1 and 2 Hz is tightly constrained in the CWT scalogram whilst maintaining high temporal resolution across the pulsatory signal energy.

4 APPLICATION OF CWT TO SANTIAGUITO BROADBAND SEISMIC DATA

In this section, we evaluate the application of CWT spectral analysis to data recorded during two campaign studies at Santiaguito volcano in Guatemala (Fig. 4). For consistency, we follow the nomenclature for volcano-seismic frequency bands used in previous studies at Santiaguito (e.g., Johnson et al., 2009; Sanderson et al., 2010): ultra-long-period (ULP, 600 – 30 s period), very-long-period (VLP, 30 – 5 s period), long period (LP, 5 – 1 s period), short period (SP, 1 – 10 Hz) and high frequency (HF, 10 – 50 Hz).

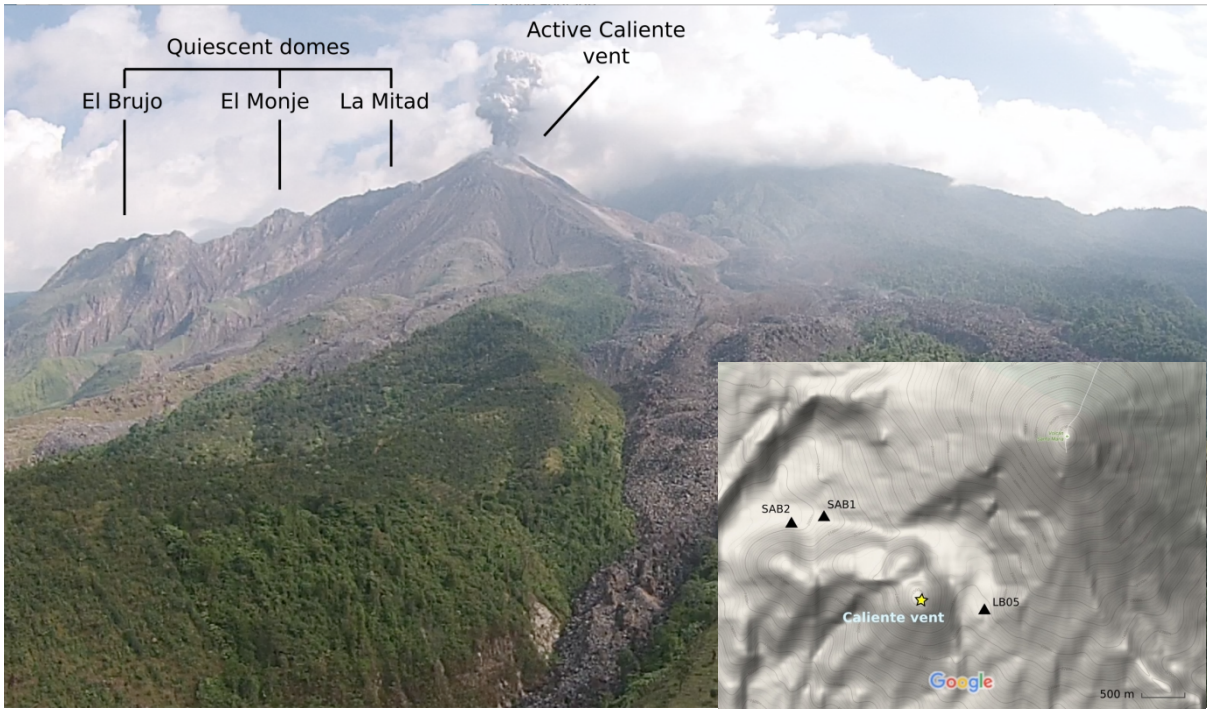

Figure 4 – Main: Santiaguito volcanic dome complex. *Photograph taken from aerial drone to the south. Santa María (parent stratovolcano) is obscured by clouds in the background.* ***Insert: Map of seismic stations used in this study.*** *Map data copyright Google 2016.*

Santiaguito is a volcanic dome complex growing out of the large explosion crater left by the cataclysmic 1902 plinian eruption of Santa María, one of the largest eruptions of the 20th century in both magnitude and estimated loss of life (Rose, 1972; Williams and Self, 1983). The easternmost Caliente vent (Fig. 4) has been in a (partially) 'open-vent' state for several decades (Harris et al., 2003), with continuous blocky lava extrusion and intermittent but frequent gas-and-ash explosive eruptions (De Angelis et al., 2016; Holland et al., 2011). Although the underlying mechanism behind Santiaguito's frequent eruptions is still subject to some debate, these small-scale explosive eruptions are characterised by increased rates of

precursory dome inflation (Johnson et al., 2014), 30 to 60 s of vigorous emissions (Bluth and Rose, 2004) and pre/syn-eruptive HF, VLP and ULP seismicity (Johnson et al., 2014, 2009; Sanderson et al., 2010).

We focus first on ULP events, which have been observed to accompany strombolian (Genco and Ripepe, 2010), phreatic (Aoyama and Oshima, 2008) and small pyroclastic explosions (Johnson et al., 2009; Sanderson et al., 2010) and are thought to represent pre/syn-eruptive deformation of the volcanic edifice. ULP signals tend to appear most strongly on the horizontal components of broadband seismometers, consistent with a change in apparent acceleration due to rotation of the instrument's horizontal axes with respect to the direction of gravity (Genco and Ripepe, 2010; Wielandt and Forbriger, 1999). The common occurrence of syn-eruptive ULP signals makes Santiaguito an ideal system at which to assess the CWT's ability to capture and characterise simultaneous signal features over wide-ranging frequency scales, including both the VLP to ULP range (600 – 5 s period) and SP to HF range (1 – 50 Hz), as well as its ability to analyse eruption-related volcano-seismic data.

4.1 STATION LB05

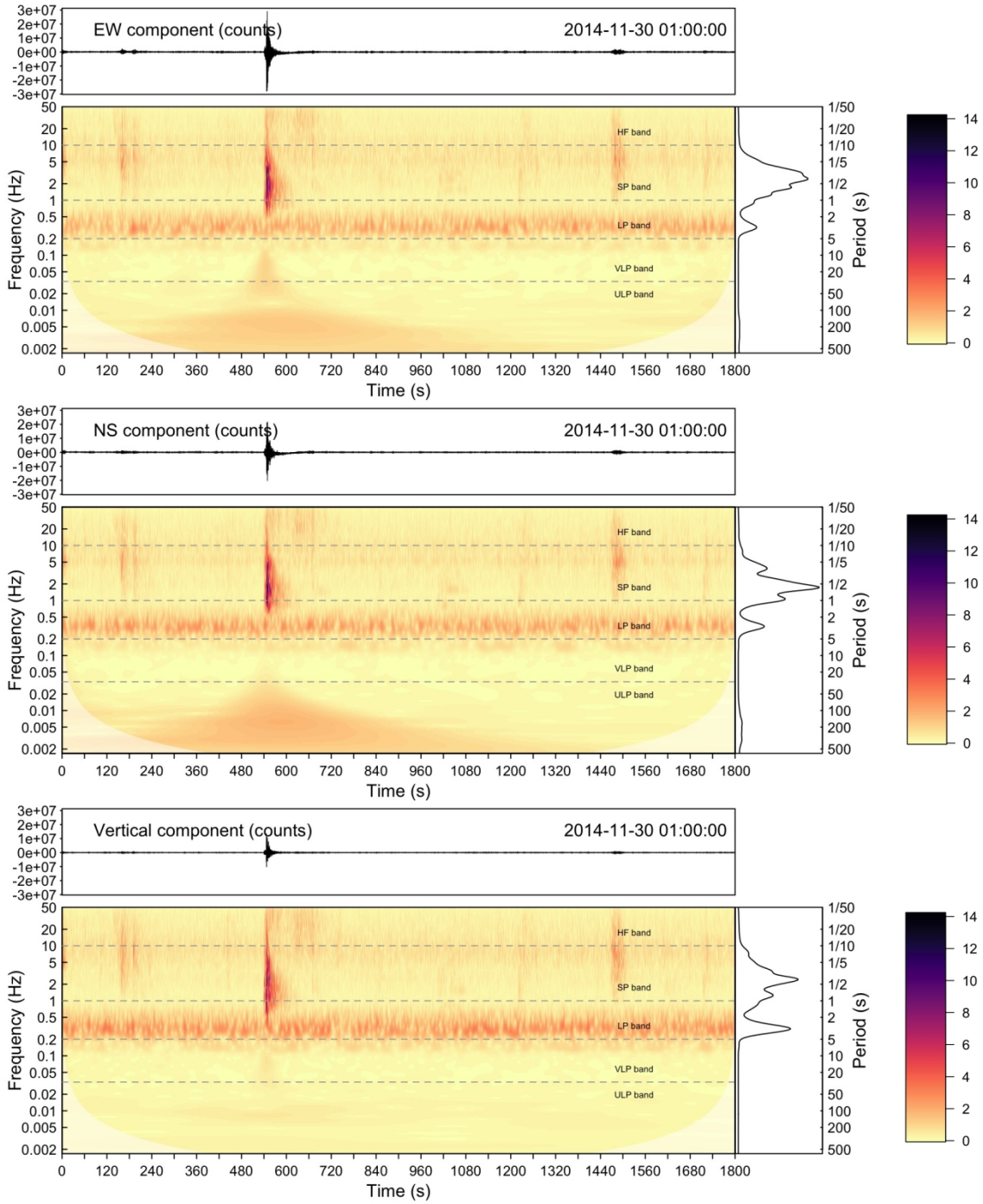

Figure 5 –Three-component 'broadband' scalograms for typical eruption at Santiaguito (station LB05). *Top: scalogram for near-radial EW component with clearly discernible energy in VLP (5 to 30 s period) and ULP (30 to 600 s period) spectral ranges. Middle: scalogram for NS component with discernible energy in ULP range, but not VLP range. Bottom: scalogram for vertical component with no discernible energy in ULP or VLP ranges. Clear band of double-frequency (DF) ocean microseisms in LP range on all three components. Time duration in each scalogram is 30 minutes. Average wavelet power distribution plots on right hand side help identify spectral peaks. Scale bars for CWT amplitudes (with fourth-root scaling) given on far right. All scalograms produced with Morlet wavelet (ω_0 = 6) and fourth-root amplitude scaling and all plot limits are equal across the three components.*

The first set of seismic data from Santiaguito comprises a continuous 24-hour section of seismic data collected by the School of Environmental Sciences, University of Liverpool, on 30th November 2014 (station LB05, Fig. 4). LB05 hosted a 3-component Nanometrics Trillium 120 s broadband seismometer sampled at 100 Hz and oriented with the east-west (EW) axis approximately radial to the active Caliente vent. The proximity of the instrument to the vent (approximately 800 m) provides high SNR ideal for detecting pre/syn-eruptive VLP and ULP signals beyond the instrument corner frequency and related to inflation-deflation and inferred pressurisation dynamics seen in previous studies (e.g., Johnson et al., 2009; Sanderson et al., 2010).

Instrument response deconvolution was undertaken (e.g., Haney et al., 2012) but led to a consistent very-long-period nonlinear impulse response due to shaking following each explosion (e.g., Delorey et al., 2008). This apparent impulse response appears to mask the more pertinent ULP rotational signal components related to the inflation/deflation dynamics of the volcanic edifice, particularly those prior to each explosion, which are tiny in magnitude by comparison. Given that a broadband seismometer's response to tilt dominates over its response to translational motion at frequencies well below its corner frequency (e.g., Genco and Ripepe, 2010), and we are not attempting to recover the full amplitude of very-long-period translational displacement signals (e.g., for full waveform inversion or moment tensor estimation), we do not perform instrument response deconvolution in any of the examples throughout this study.

Broadband scalograms (i.e., 600 s period to 50 Hz) reveal a 2 – 4 s period site noise running throughout (Fig. 5, all three components), consistent with global seismic noise levels from double-frequency (DF) deep ocean and near-coastal microseisms (Bromirski et al., 2013; Koper and Burlacu, 2015). This band of 'noise' effectively (and conveniently) divides the spectra into two parts: SP-HF frequencies (1 – 50 Hz) and VLP-ULP frequencies (5 – 600 s period). It also provides a scale for basing the relative energy of other frequency bands, which can be useful in automated event classification (e.g., Hibert et al., 2017).

Over the 24-hour period, 27 explosion events were identified through manual inspection of raw seismic and pseudo-tilt traces. Pseudo-tilt (e.g., Genco and Ripepe, 2010) was derived by: i) converting units in the raw seismic velocity signal from counts to m/s and integrating to displacement; ii) low-pass filtering below the corner frequency (1/120 Hz); and iii) multiplying

filtered displacement by $(2\pi f_0)^2/g$, where f_0 is the instrument corner frequency (in this case, 1/120 Hz) and g is the gravitational constant $\approx$ 9.81. The explosive eruptions recorded by instrument LB05 show self-similar seismic characteristics and are readily identifiable from CWT scalograms. Both horizontal components show syn-eruptive ULP signals with periods of around 100 to 500 s. These are clearly visible in the VLP-ULP half of the scalograms in Fig. 5 (EW and NS components only) as 'dark patches' and are easily distinguishable from atmospheric VLP-ULP noise or other volcanic events by their distinctive funnel shapes. Given that explosions are characterised by both high inflation and deflation rates (Johnson et al., 2014), a sharp change in velocity signal at the point of inflation-deflation transition likely explains this distinctive funnel shape. Indeed, this feature is highlighted when the CWT is restricted to just the VLP-ULP range (Fig. 6). Syn-eruptive ULP signals are absent or barely discernible on the vertical component, with dominant energy on the horizontal components below the instrument corner frequency, confirming that they are the result of tilt, and therefore inflation-deflation dynamics of the volcanic edifice, rather than translational horizontal ground motion (Wielandt and Forbriger, 1999).

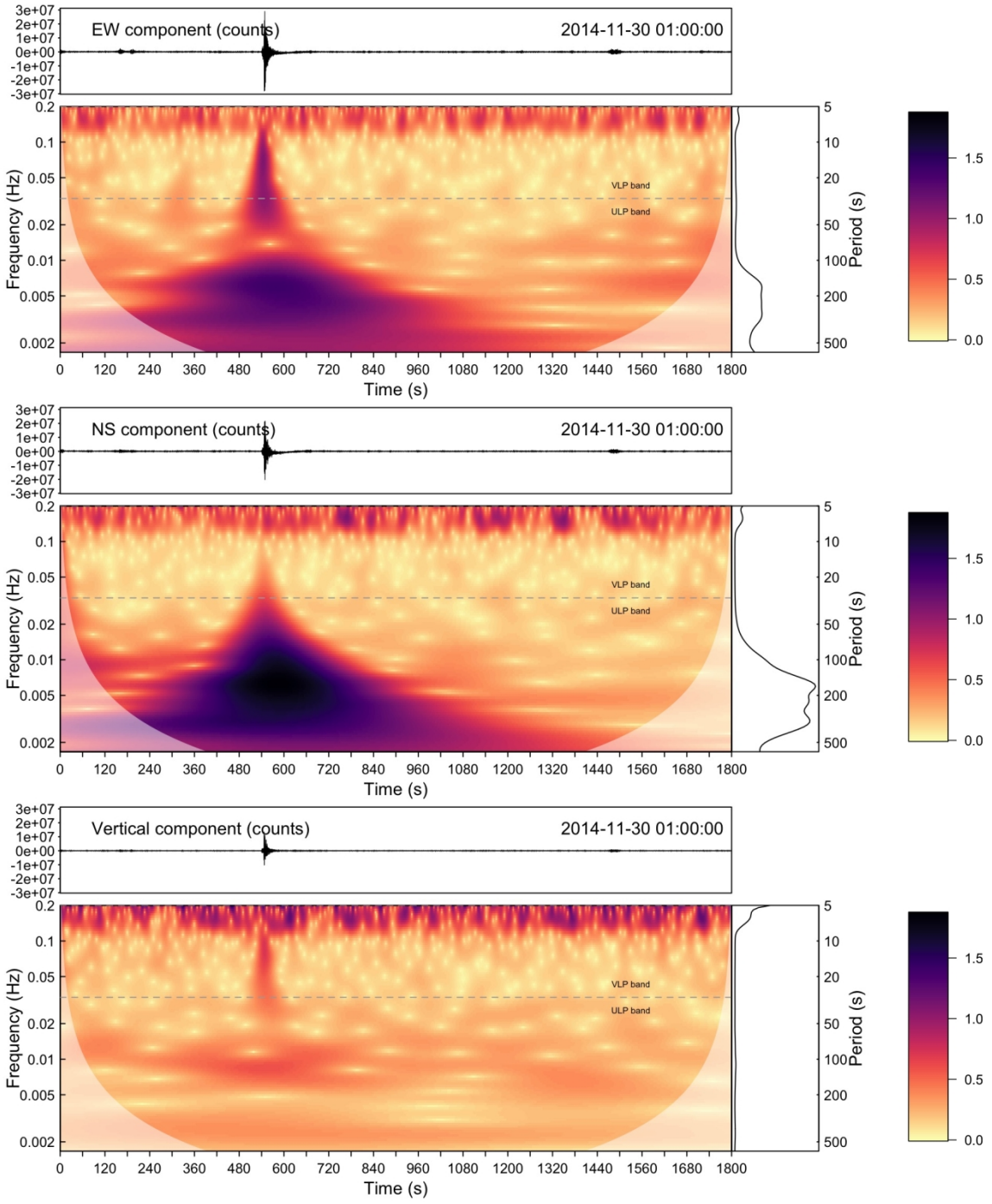

Figure 6 –Three-component scalograms for same signal segment as Fig. 5, with spectral range restricted between 5 s and 600 s periods. *VLP/ULP event dominates spectra on horizontal components but is practically indiscernible on the vertical component. Time duration in each scalogram is 30 minutes. Scale bars for CWT amplitudes (with fourth-root scaling) given on far right. All scalograms produced with Morlet wavelet (ω_0 = 6) and all plot limits are equal across the three components.*

The near-radial EW component also consistently detects a spectrally distinct shorter-period syn-eruptive VLP-ULP signal (typically between 6 and 64 s), which is not present on the north-south (NS) component and is strongly centred on main explosion onset throughout this dataset. The response of the seismometer to both tilt and translational motion is relatively equal within

this spectral range (Genco and Ripepe, 2010), particularly as you move towards the instrument's corner frequency (in this case, 1/120 Hz), so it would be extremely difficult to deconvolve these two components of motion to determine source without reference from an independent tiltmeter or greater seismic array coverage.

The effective width of the wavelet used (central frequency $\omega_0 = 6$) in Figures 5 and 6 is too long at ULP scales, both in timescale and number of oscillations, to accurately characterise the nature and onset times of these ULP signals. Such long-period low- (or non-)oscillatory features can be better characterised through use of a Morlet wavelet with a very low central frequency (Addison et al., 2002). At central frequencies down to $\omega_0 \approx 1$, the real part of the complex Morlet wavelet resembles a dampened Ricker wavelet and the imaginary part resembles a tapered single cycle of a sine curve (Fig 3 bottom left). The real and imaginary parts therefore bear a strong similarity to the second order derivative and negative of the first order derivative of a Gaussian function, respectively (Shao and Ma, 2003). As such, their wavelet transforms provide smoothed (or 'denoised') approximations of the signal's first and second order derivatives in the T-F domain (Nie et al., 2002; Shao and Ma, 2003; Fig 7). Such low-oscillatory wavelets are also deemed more 'temporal' in their characterisation of the signal than spectral (Addison et al., 2002), providing greater temporal resolution at the cost of reduced frequency resolution.

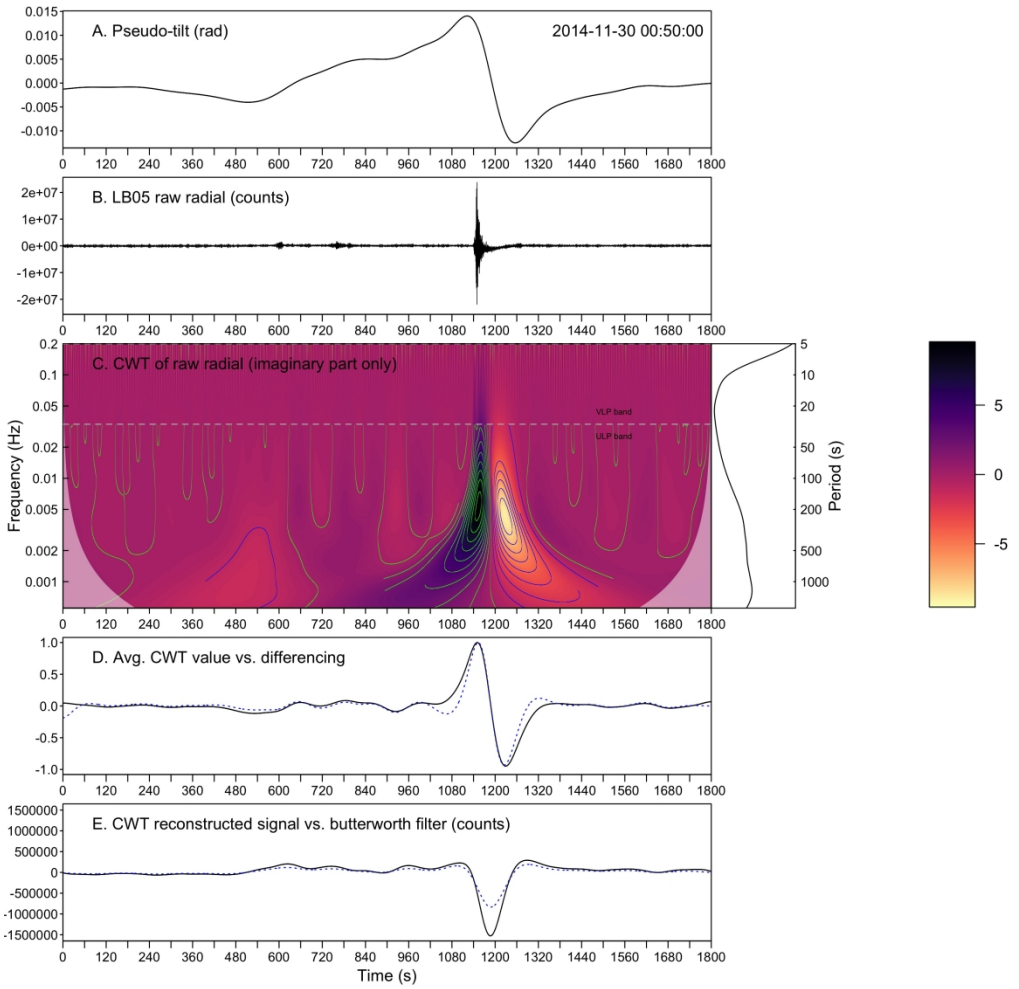

Figure 7 – Examination of explosion event in Figs 5 and 6 with low-oscillation Morlet wavelet, ω_0 = 1. *A) Radial component pseudo-tilt trace derived following method of Genco and Ripepe (2010). B) Raw seismic trace rotated to radial component. C) CWT scalogram (imaginary part only) using Morlet wavelet, ω_0 = 1. D) Scale-averaged CWT values (self-normalised, solid black line) and negative of bandpass filtered first-order differencing (lag = 2, self-normalised; dashed blue line) between 120 and 1800 s. E) CWT reconstructed signal (solid black line), following Torrence and Compo (1998), and 2-pass 2-pole Butterworth bandpass filtered signal (dashed blue line) between 30 and 1800 s. CWT scalogram restricted between 5 s and 1800 s periods. Green and blue contour lines added in ULP range of scalogram to show regions of strongest positive and negative wavelet-signal similarity, respectively. Time duration in scalogram is 30 minutes. No amplitude scaling applied to CWT scalogram, with scale bar given on far right.*

Figure 7 examines the explosion signal in Figures 5 and 6 through the lens of a low-oscillation Morlet wavelet ($\omega_0 = 1$). The original horizontal components have been rotated 20 degrees so that they are radial and tangential to the active Caliente vent. The main ULP signal now manifests as an 'up-down' feature in the time domain (i.e., a region of strong positive value followed by a region of strong negative value) with spectral period of around 200 s on the radial component scalogram in Figure 7C, centred around 1200 s along the horizontal time axis. This can clearly be seen in the scale-averaged CWT values, which have been restricted between periods of 120 and 1800 s, in Figure 7D (solid black line) – as expected, these scale-averaged values provide a close approximation to first-order differencing within this frequency

range (Fig 7D dashed blue line). The wider peaks in the CWT approximation of the first-order derivative are likely due to the poorer frequency resolution of low-oscillation wavelets at such long periods. The ULP onset time (largest amplitude part of dark region, indicated by green contour lines in Fig 7C) appears to be approximately coincident with the explosion event itself, which can be more clearly seen in the reconstructed (or, effectively, filtered) signal given in Figure 7E (solid black line), derived by summing the real part of the CWT and scaling through a combination of signal sample rate, wavelet scale resolution and wavelet-specific reconstruction factors to preserve signal energy (Torrence and Compo, 1998), between 30 and 1800 s periods. The reconstructed signal at these long periods appears to exaggerate the strength of these ULP components when compared against a 2-pass Butterworth filter over the same frequency range (Fig 7E dashed blue line), albeit with similar waveform structure.

There is also a weaker, lower frequency ULP spectral component (approx. 0.001 Hz) in the CWT scalogram (Fig 7C) at around 480 s on the horizontal time axis, approximately 10 minutes before explosion. This component is coincident with the start of an upward trending inflation signal in the pseudo-tilt trace (Fig 7A), typical of explosions at Santiaguito and thought to relate to tilt as a result of volumetric change of a shallow Mogi-type source (e.g., Johnson et al., 2014, 2009). The method of extracting tilt signals from broadband seismometers can be controversial as long-period signals before a high amplitude impulse can be an artefact of low-pass acausal filtering (Lyons et al., 2012). However, the presence of this isolated, coincident ULP signal in the scalogram (Fig 7C), derived independently from the raw velocity signal, confirms that this apparent inflation process prior to eruption is not an artefact of signal processing. This precursory ULP also coincides with the start of an oscillatory feature in the reconstructed, or filtered, signal (Fig 7E) and average CWT values (i.e., first-order derivative; Fig 7D). The pre-eruptive oscillatory feature is weak but just visible in the CWT scalogram (no amplitude scaling; Fig 7C) between periods of 30 and 200 s. Changes in seismic activity prior to eruptions at Santiaguito, associated with increased fumarolic jetting and opening of near-surface fractures, have been observed previously (Johnson et al., 2009). However, without further instrumentation (seismic, video, infrasound) it is impossible to determine cause in this case.

The SP-HF components (1 – 50 Hz) of explosion events in this dataset typically last around 1 minute, which is consistent with timescales of vigorous emissions (e.g., Bluth and Rose, 2004). The corresponding explosion signals in the LP, SP and HF ranges (5 s period to 50 Hz) are best examined through a ‘zoomed-in’ scalogram, produced by restricting the time and period ranges

in computation of the wavelet transform itself (Fig. 8). These ‘zoomed-in’ scalograms also show self-similar eruption characteristics throughout the dataset, with high SNR, emergent onset, stronger broadband energy arrival (0.5 – 16 Hz) after ~ 5 s, rapidly attenuating higher frequency components, and LP-style resonance in the coda (roughly 1 – 3 Hz). Spectral peaks are generally found between 0.5 and 4 Hz on all three components and there are often two or three distinct high-energy components. This inter-eruptive self-similarity means explosion events can, in principle, be both manually and automatedly identified through use of appropriate CWT characteristics (e.g., Hibert et al., 2017).

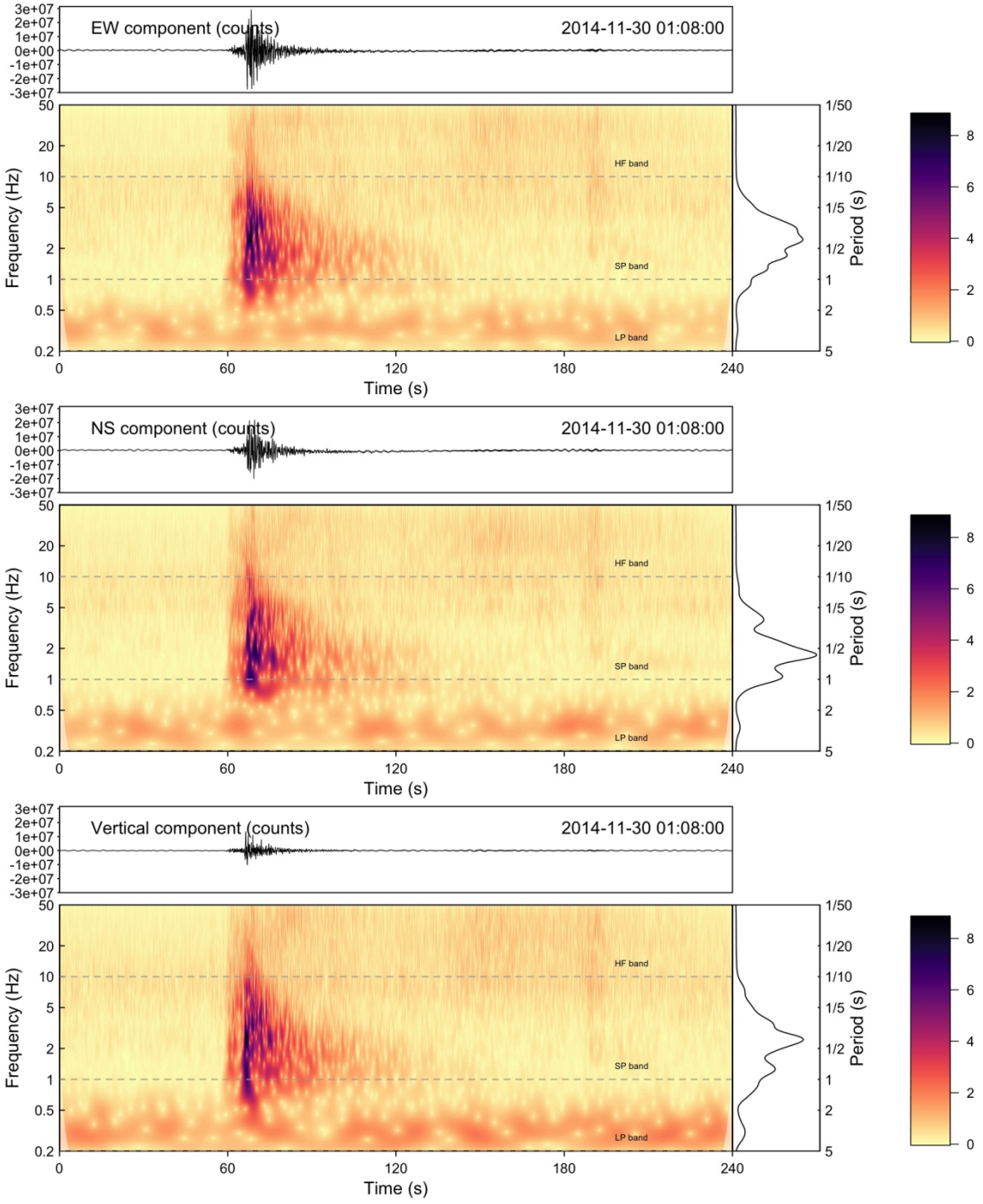

Figure 8 –Three-component scalograms for explosion event in Fig. 5, with spectral range restricted between 50 Hz and 5 s period. *Time duration in each scalogram is 4 minutes. All scalograms produced with Morlet wavelet ($\omega_0 = 6$) and fourth-root amplitude scaling and all plot limits are equal across the three components.*

4.2 DATA FROM 'WORKSHOPS ON VOLCANOES 2016'

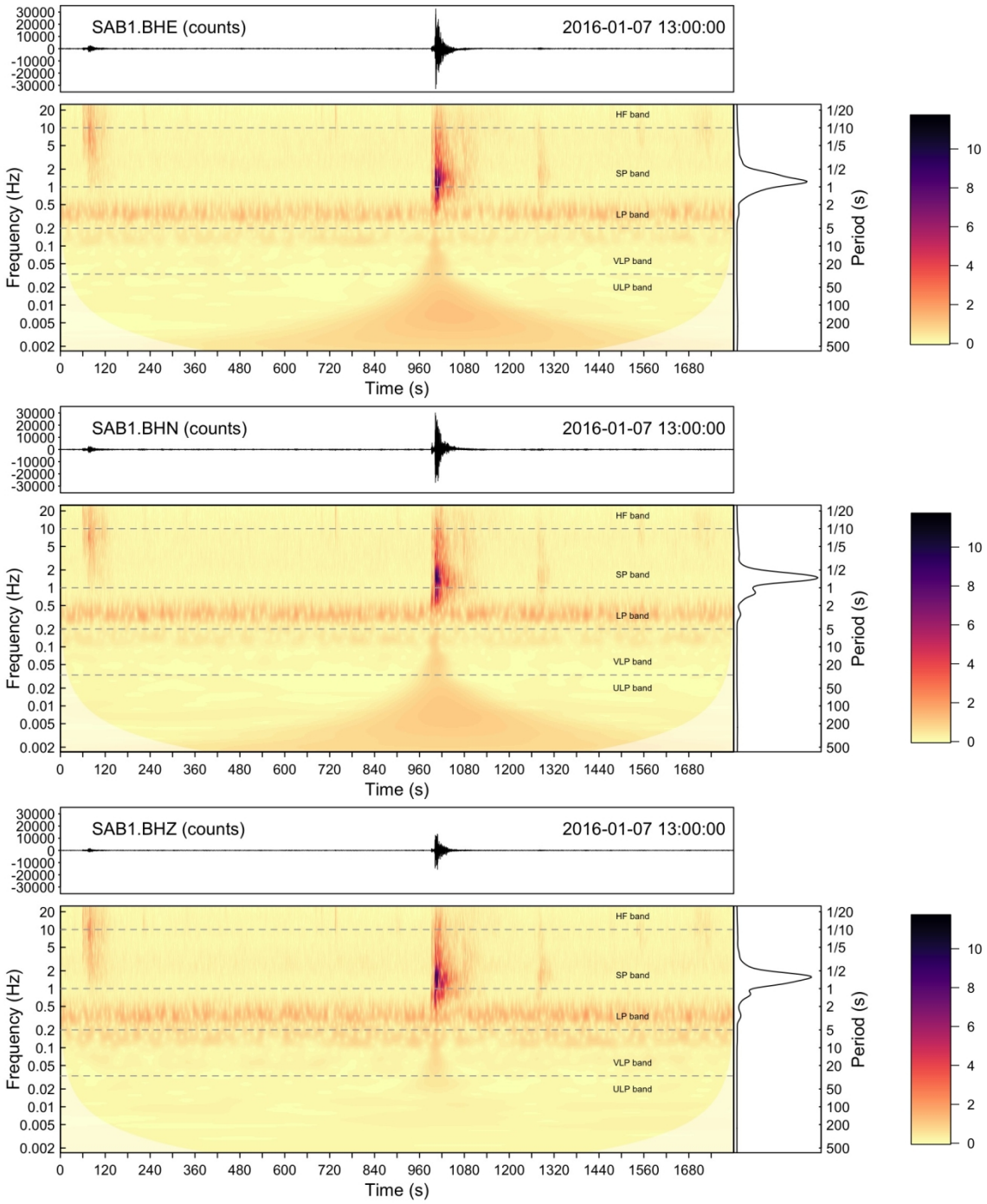

Figure 9 – Three-component 'broadband' scalograms for typical eruption during Workshops on Volcanoes at Santiaguito, January 2016 (station SAB1). *Top: scalogram for EW component with discernible energy across VLP and ULP spectral ranges (dark 'funnel' shape). Middle: scalogram for NS component with similar VLP/ULP energy as EW component. Bottom: scalogram for vertical component with no discernible energy in ULP range. Average wavelet power distribution plots on right hand side reveal fewer spectral peaks in LP-SP range than during previous deployment (station LB05; Fig. 5). Time duration in each scalogram is 30 minutes. All scalograms produced with Morlet wavelet ($\omega_0 = 6$) and fourth-root amplitude scaling, and all plot limits are equal across the three components.*

The second dataset obtained for Santiaguito consists of a 48-hour continuous recording of seismic data from two instruments deployed over a 10-day period in January 2016 (stations SAB1 and SAB2 in Fig. 4; McKee et al., 2015). These data are available through the IRIS Data Management Center (see Acknowledgements). A catalogue of eruption times, confirmed either visually or through infrasound, and other detected seismic events over the 48-hour period was developed by the authors. Both instruments were 3-component Nanometrics Trillium Compact PH broadband seismometers, with corner frequencies of 120 s and dataloggers set to 50 Hz continuous sampling. The instruments were located approximately 1.5 – 1.9 km north-west of the active Caliente vent and were expected *a priori* to yield lower amplitude signals with greater complexity due to attenuation and local/path effects (Anderson et al., 2012).

The events in this dataset are generally characterised by lower SNR with prevalent ULP noise (> 32 s period) throughout. The 2 – 4 s period noise seen in the data from LB05 in November 2014 manifests as 2 – 8 s period noise in this dataset (Fig. 9), which is still consistent with global ambient microseisms from deep ocean and near-coastal waves (Koper and Burlacu, 2015). Despite considerable background noise, lower amplitude events are still generally discernible in scalograms without pre-processing or filtering.

In total, 18 explosive eruptions had been previously confirmed visually or through infrasound. These were all initially examined using 30-minute broadband scalograms (600 s to 25 Hz; e.g., Fig. 9) for both stations, SAB1 and SAB2. Of these 18 confirmed eruptions, scalograms for station SAB1 show 14 clear syn-eruptive ULP signals, of which 8 have both syn-eruptive ULP and VLP signals consistent with previous eruption characteristics, and with similar SP-HF band to VLP-ULP band energy ratios. By comparison, only 7 syn-eruptive ULPs, with much lower amplitude, are initially visible on broadband scalograms for SAB2, of which only two exhibit both syn-eruptive ULP and VLP signals. However, when scalograms are restricted to the VLP-ULP period range (600 s – 5 s period), the number of visible ULPs at SAB2 increases to 14, with 8 coincident VLPs (the same as at SAB1). It must be noted, however, that the manner in which ULPs are deemed ‘visible’ in scalograms is obviously subject to chosen amplitude scaling (here fourth-root scaled and self-normalised by maximum amplitude across all three components).

In contrast to data from the previous deployment (Results 4.1), the dominant energy of ULPs at SAB2 is not always coincident with eruption onset; one such ULP signal appears to occur

minutes after the onset of an explosion event (Fig. 10), with a period of around 150 - 200 s (time $\approx$ 1320 s). This is related to a sharp upward (inflation) trend in the pseudo-tilt trace after the typical initial transition from steady inflation to sharp deflation around explosion onset (Fig. 10A; time $\approx$ 1000 s). This earlier transition has a lower spectral period of around 400 s and weaker spectral amplitude (Fig. 10C). Explosions at Santiaguito are regularly followed by secondary explosions (on the order of 1 – 3 minutes), so a reasonable, yet speculative, explanation for the cause of this later ULP component and sharp upward trend is that it reflects priming of a secondary explosion or more minor degassing. However, further source modelling and verification is not possible due to limited instrument coverage. Both the inflation-deflation transition around explosion onset and this later secondary feature are clearly visible in the first-order derivative (Fig. 10D solid black line) and CWT reconstructed (Fig. 10E solid black line) traces. As with the event in Figure 7, a weaker, even longer period ULP component (around 1000 s period), coincident with the start of an upward inflation trend in the pseudo-tilt trace, is visible in the CWT scalogram (time $\approx$ 400 s). It is evident that such ULP feature characterisation differs greatly from other seismic event types and could potentially be used to predict an upcoming explosion given that CWT scalograms with a low-oscillation wavelet do not require signal lengths significantly longer than the spectral component under examination.

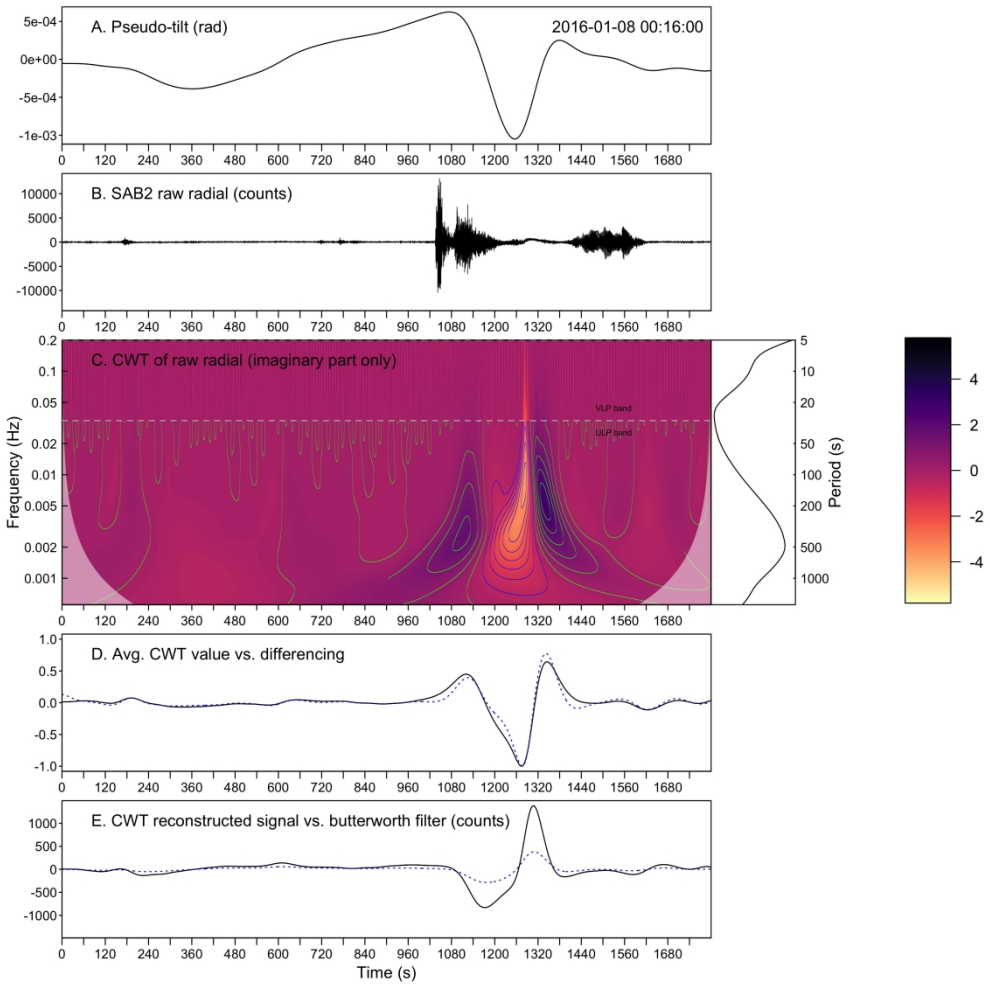

Figure 10 – Examination of explosion event and 'late' ULP with low-oscillation Morlet wavelet, $\omega_0 = 1$. *A) Radial component pseudo-tilt trace. B) Raw seismic trace rotated to radial component. C) CWT scalogram (imaginary part only) using Morlet wavelet, $\omega_0 = 1$. D) Scale-averaged CWT values (self-normalised, solid black line) and negative of bandpass filtered first-order differencing (lag = 2, self-normalised; dashed blue line) between 120 and 1800 s. E) CWT reconstructed signal (solid black line), and 2-pass 2-pole Butterworth bandpass filtered signal (dashed blue line) between 30 and 1800 s. CWT scalogram restricted between 5 s and 1800 s periods. Green and blue contour lines added in ULP range to show regions of strongest positive and negative wavelet-signal similarity, respectively. Time duration in scalogram is 30 minutes. No amplitude scaling for CWT scalogram, with scale bar given on far right.*

The presence of ULPs/VLPs at these stations is surprising in itself, as both were believed to be outside the geographic range (around 1.1 km) of these signals at Santiaguito (Sanderson et al., 2010). One possible explanation is that the whole dome complex, and not just the dome associated with the active Caliente vent, undergoes some degree of inflation-deflation. To validate the source location of these signals, the SAB1 data were rotated 132 degrees so that the horizontal components were aligned radially and tangentially to the Caliente vent. The ULP and VLP signals now appear solely on the radial component (Fig. 11), suggestive of tilt resulting from a previously modelled shallow Mogi-type source located directly beneath or

northwest of the active Caliente vent (i.e., along the radial axis from vent to instrument; e.g., Johnson et al., 2009; Sanderson et al., 2010; Wiens et al., 2005).

The VLP-ULP signals in this later dataset are more complex than those recorded in the earlier dataset (Fig. 11), with an initial shorter-period upward 'spike' in the VLP range, followed by the same characteristic convex bump in the ULP range seen previously. While not visible in the pseudo-tilt trace or first-order signal derivative (both restricted below 120 s period), this initial spike is clear in the CWT reconstructed signal (Fig. 11E solid black line) and visible in the VLP range of the CWT scalogram when plotted over a shorter time period. Unlike Figures 7 and 10, a precursory ULP feature marking the start of an upward inflation trend in pseudo-tilt is not readily identifiable across the various CWT traces in Figure 11; however, it may have an even longer spectral period of > 1800 s, or its spectral amplitude may be too weak to see without amplitude scaling.

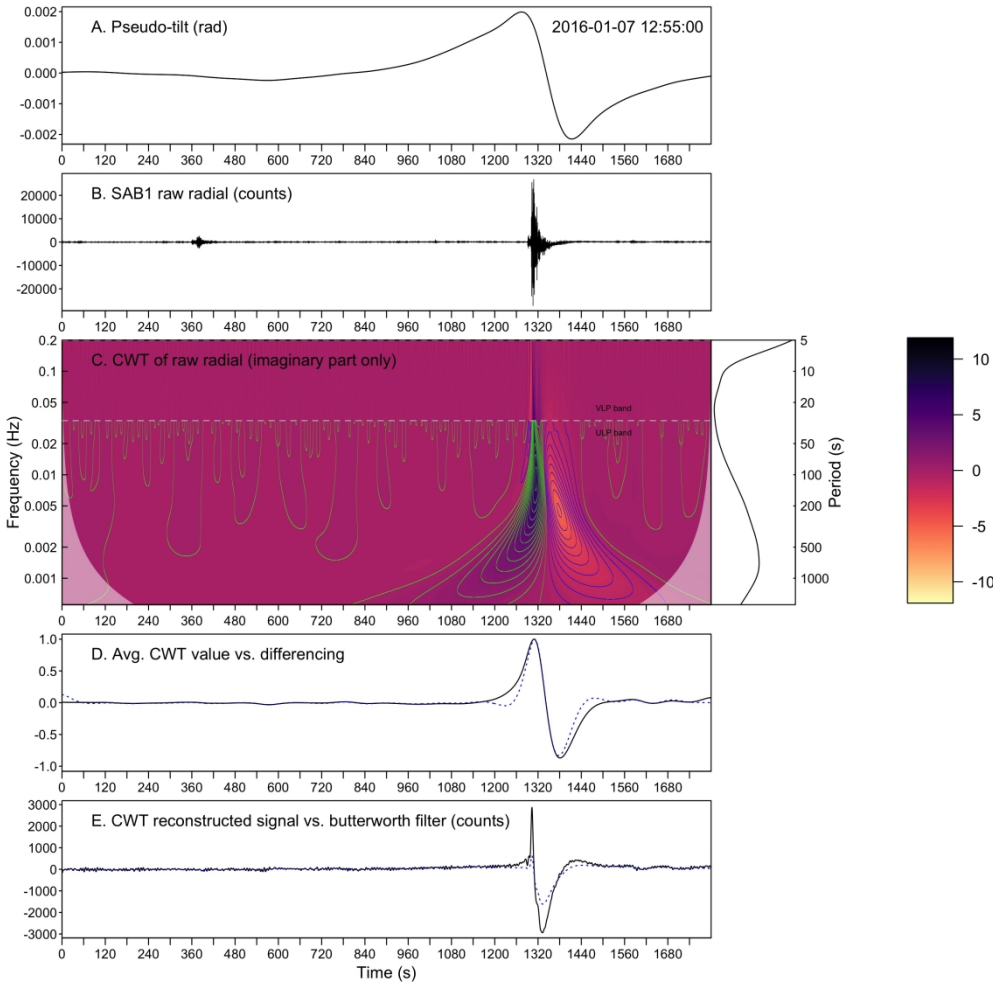

Figure 11 – Examination of explosion event in Figure 9 with low-oscillation Morlet wavelet, $\omega_0 = 1$. *A) Radial component pseudo-tilt trace. B) Raw seismic trace rotated to radial component. C) CWT scalogram (imaginary part only) using Morlet wavelet, $\omega_0 = 1$. D) Scale-averaged CWT values (self-normalised, solid black line) and negative of bandpass filtered first-*

order differencing (lag = 2, self-normalised; dashed blue line) between 120 and 1800 s. E) CWT reconstructed signal (solid black line), and 2-pass 2-pole Butterworth bandpass filtered signal (dashed blue line) between 5 and 1800 s. CWT scalogram restricted between 5 s and 1800 s periods. Green and blue contour lines added in ULP range to show regions of strongest positive and negative wavelet-signal similarity, respectively. Time duration in scalogram is 30 minutes. No amplitude scaling for CWT scalogram, with scale bar given on far right.

Seismic characteristics of explosions within the SP-HF range (1 – 25 Hz) show far greater variability during this deployment (Fig. 12). Explosions that produce the clearest VLP-ULP signals have similar SP-HF seismic characteristics to those recorded in the previous deployment (Results 4.1), although with sharper onsets, longer duration dominant energy and longer resonance in the coda. Additionally, these signals are often complicated by post-eruptive tremor 'bursts' and rockfalls that are characteristically distinct from explosion signals in CWT scalograms. Spectral peaks are more tightly focused between 1 and 2 Hz, most likely the result of path effects and greater attenuation due to greater hypocentral distances between vent and instruments. Seismic characteristics from some explosions may be difficult to discriminate from other (probably co-occurring) events, such as rockfalls and harmonic bursts (Fig. 12), but can often be identified by the presence of ULP +/- VLP signals.

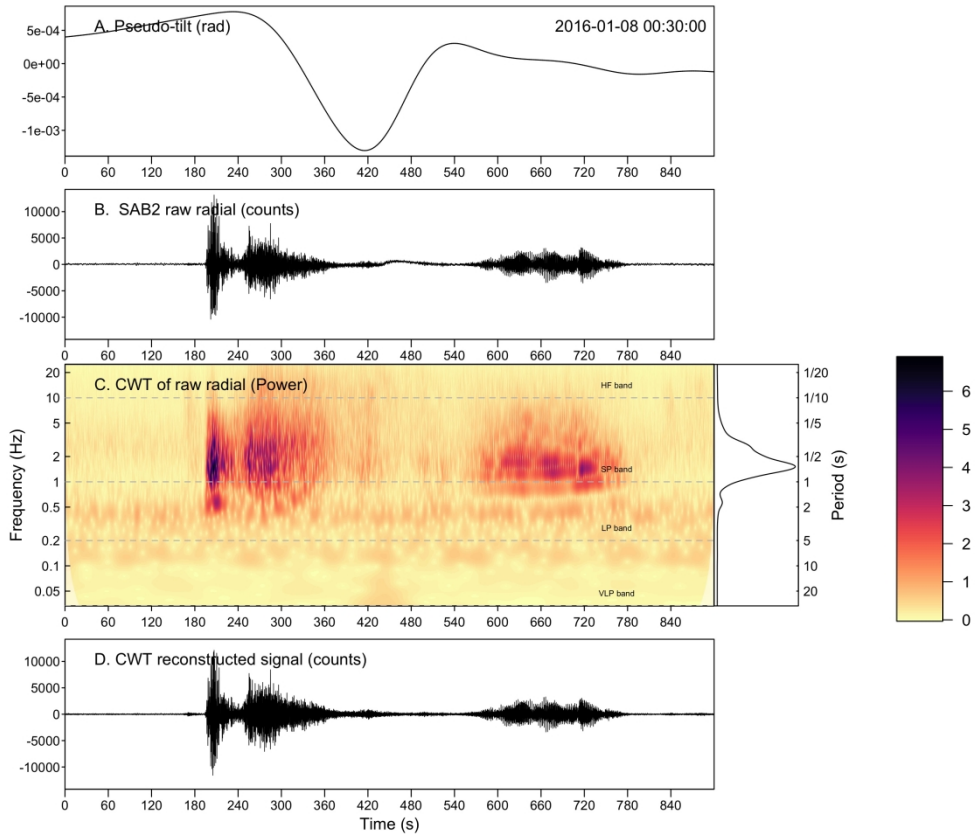

Figure 12 – Complicated higher frequency explosion signal in Fig. 10. *A) Radial component pseudo-tilt trace. B) Raw seismic trace rotated to radial component. C) CWT scalogram (power) using complete Morlet wavelet, ω_0 = 6. D) CWT reconstructed signal (solid black line) between 1/30 and 25 Hz. CWT scalogram restricted between 30 s period and 25 Hz.*

Time duration in scalogram is 15 minutes. CWT scalogram produced with fourth-root amplitude scaling, with scale bar given on far right.

5 DISCUSSION

5.1 COMPARISON OF CWT SCALOGRAMS AND STFT SPECTROGRAMS

Modern volcano seismology focuses largely on pattern recognition in volcano-seismic signals, and modelling source mechanisms based on waveform shapes. Thus any spectral analysis tool in volcano seismology must be able to fully characterise the various attributes of seismic signals and discriminate them from background noise. Moving window spectrograms in McNutt and Roman (2015) adequately decompose signals into T-F space within a relatively tight band of interest (1 – 10 Hz). When compared with CWT scalograms, however, the shortcomings of these spectrograms, even within this tight window, become apparent. Most notably, the short window lengths used to achieve high time resolution in the STFT spectrograms sacrifice frequency resolution: spectral peaks are less constrained in the STFT frequency distributions than in the CWT scalogram equivalents (e.g., Figs 2B, F, G and H). Similarly, longer STFT window lengths, required to encompass VLP and ULP signals, sacrifice a great degree of time resolution (e.g., Fig 2C), and window lengths would need to be very long (on the order of hundreds or even thousands of seconds) to adequately characterise the ULP signals observed throughout this study. The use of such long window lengths also comes with greater computational cost and memory requirements. Figure 13 shows a comparison of computational times between the STFT and CWT approaches for varying signal lengths and number of STFT frequency components (or, equivalently, wavelet scales). A noisy signal with two main sinusoidal components was generated at different signal lengths (a doubling in length from 400 to 254800 samples; Fig. 13A) and median computational time from 5 runs plotted for varying number of frequency components, STFT window lengths and levels of STFT overlap. STFT spectrograms were computed using a standard R routine (*signal::specgram*) and CWT scalograms, with equivalent outputs, were computed using the code in Appendix 1.

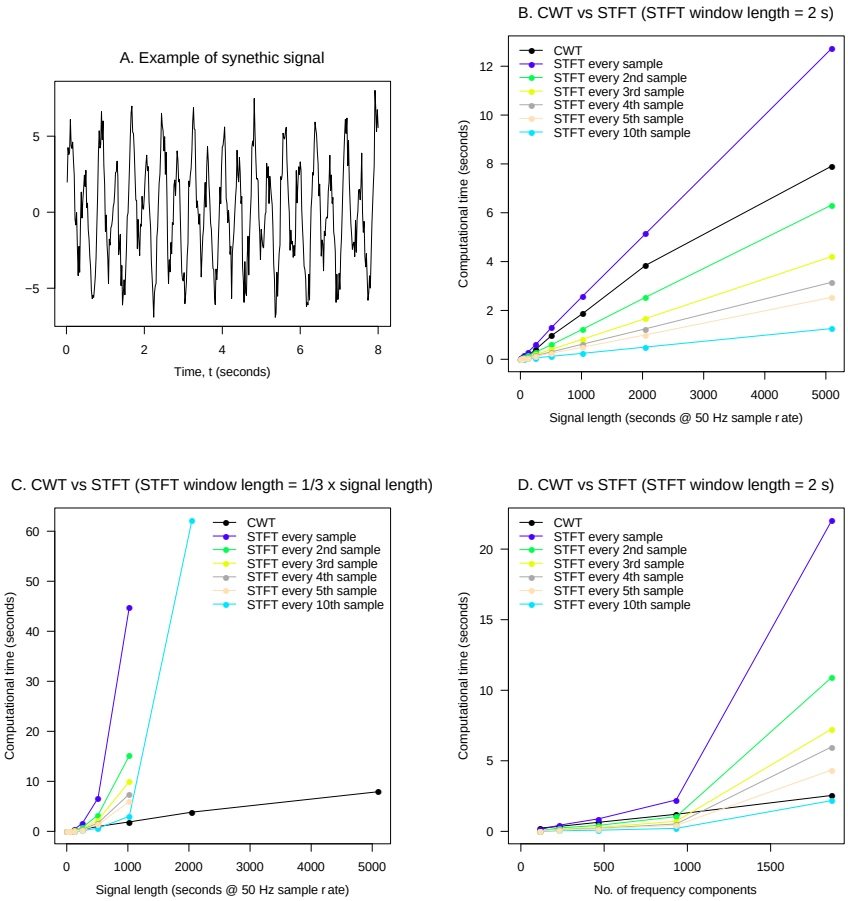

Figure 13 – Comparison of computational times between CWT and STFT. *A) Example of synthetic signal with 50 samples per second used for comparisons ($f(t) = 4sin(16t) + 2sin(8t) + \varepsilon$; $\varepsilon \sim N(0,1)$). B) Comparison of CWT and STFT with fixed window length (2 s) for varying signal lengths and levels of STFT overlap. C) Same as B) but with varying STFT window length (1/3 x signal length in seconds). Missing points are due to computational operation exceeding memory size. D) Comparison of CWT and STFT with fixed window length (2 s) for varying number of STFT frequencies / wavelet scales and levels of STFT overlap (signal length fixed at 128 s, or 6400 samples). All points in plots are the median from 5 runs, computed on a 2017 iMac with 4.2 GHz Intel Core i7 and 16 GB memory.*

When the STFT is conducted at every sample point in a signal with the number of STFT frequency components equal to number of CWT wavelet scales, the resulting outputs from the CWT and STFT approaches are of equal dimension (*no. of frequencies* $\times$ *no. of samples in signal*). Under this condition, Figures 13B and C show that the CWT has lower computational cost than the STFT for all signal lengths (no. of frequency components all equal, $n_f = 234$). However, the advantage of the STFT's moving window approach is that it need not be conducted at every sample point and can, instead, be conducted at every n^{th} sample point. Such a step reduces computational time by a factor of n for fixed window lengths (Fig. 13B), with the size of the resulting output transform matrix also reduced by a factor of n. However, this computational gain comes at the cost of reduced temporal resolution. In many cases, a coarser

representation such as this is completely sufficient and subsequent computational gains may even be necessary for time-critical processing steps. For STFT window lengths designed to capture the full spectra of a signal (i.e., down to periods equal to a third of total signal length, analogous to our CWT analysis in Section 4), the computational cost increases exponentially with signal length (Fig. 13C) and the corresponding convolutional operations can easily become too large to fit in memory (missing points at longer signal lengths in Fig. 13C), even with reduced overlap of STFT windows. By comparison, the computational cost of the CWT increases linearly with signal length, with convolutional operations on longer signals still able to fit in memory. The computational cost of increasing frequency components for STFT spectrograms increases linearly on signals of fixed length, in line with CWT scalograms, up to a point (Fig. 13C; signal length = 128 s or 6400 samples). However, when the number of frequency components computed becomes large, the computational cost of STFT spectrograms increases at a much greater rate, whilst the increase in cost from the CWT approach remains linear.

As the 0 – 1 Hz signal range in volcano seismology is becoming increasingly more of interest with the widespread adoption of broadband seismometers, a log-scaled representation is well-suited to broadband volcano-seismic spectral analysis. The CWT particularly outperforms spectrograms when representing VLPs or ULPs at frequencies well below 1 Hz. Linear-scaled spectrograms are clearly not suited to represent signals in the VLP and ULP frequency ranges (Fig. 2C, left). Even with a log-scale representation, the long window lengths needed to accommodate VLP and ULP signals greatly reduce time resolution (Fig. 2C, middle) and therefore cannot accurately characterise both high and very low frequency content. In fact, finite window length is ill-suited to a log-scale frequency representation in general, as each grid square (a function of window size and overlap) is vertically stretched at lower frequencies and vertically squeezed at higher frequencies, whilst retaining constant horizontal width, significantly reducing frequency and temporal resolution, respectively. This is the crux of the problem with Fourier transform analysis of volcano-seismic signals, and the biggest single argument for adoption of CWT analysis. That said, despite the CWT's localisation properties, there will always unavoidably be some spectral smearing in scalograms due to their over-completeness and the loose fitting of wavelet scales on either side of the true scale. This can be somewhat mitigated through frequency reassignment approaches (e.g., Tary et al., 2018), ideal for signals with isolated, narrow-band frequency components but less well-suited to signals with a continuous broadband spectrum. The CWT is also still effectively a moving

window transform so time resolution in the lower frequencies will inevitably suffer as effective window-length increases with wavelet scale. However, when compared with standard Fourier techniques, the CWT certainly performs well in both these regards.

5.2 EXTENTIONS TOWARDS AUTOMATED EVENT CLASSIFICATION AND DETECTION

The inclusion of the average energy distribution with CWT scalograms (plot on right-hand side of all scalograms and spectrograms in this study) is particularly helpful for identifying spectral peaks and distinct frequency components, which are often difficult to infer from spectrogram and scalogram images alone, or even from commonly-employed FFT amplitude plots. Importantly, the smooth appearance of CWT energy curves retains an unbiased and consistent estimation of the main spectral peaks (Percival, 1995) whilst providing superior relative weighting of dominant peaks across wide-ranging frequencies (e.g., VLP signal in Fig. 2C). The use of task-specific wavelets will correlate better with features of interest, accentuating these features in the resulting global spectra, which could potentially aid both manual and automated volcano-seismic event classification. Whilst CWT decompositions (including amplitude, phase and frequency information) have been used previously for automated event detection (e.g., Bogiatzis and Ishii, 2015; Karamzadeh et al., 2013) and more complex seismic signal filtering (e.g., Kulesh et al., 2007), we suggest that CWT attributes in general, together with their improved discrimination of important signal components and ability to characterise features across wide-ranging frequencies, would prove particularly useful in machine learning approaches to volcanic event detection and classification (e.g., Hibert et al., 2017). However, the differing characteristics between the two Santiaguito datasets illustrates that automated classification would most likely need to be not only volcano-specific but also station and activity phase specific. At the same time, subtle station-to-station or temporally evolving characteristics resulting from CWT processing can help to discriminate path effects, source mechanisms, and changes in the volcanic system over time.

6 CONCLUSION

Given the inherently varying timescales of simultaneously occurring processes at volcanic systems, from transient, localised events, such as VT earthquakes and rockfalls, to larger-scale processes, such as magma migration and deformation dynamics, the CWT's ability to match the level of detail to process scale is intuitively desirable. In the particular case of volcano-seismology, its capacity to examine/reveal spectral characteristics across a wide range of timescales make it well-suited to volcano-seismic study, where spectral components of interest can range from very short period (i.e., > 15 Hz frequency) to extremely long period (i.e., > 600 s period) signals. Furthermore, good T-F resolution across tighter bandwidths, such as the SP frequency range (1 – 10 Hz), also make it an appropriate tool for typical volcano-seismic event characterisation, especially when coupled with its corresponding distribution of average wavelet energy to reveal dominant spectral peaks.

While the utility of the CWT as a manual screening tool to aid the comprehension and exploration of volcano-seismic signals is clearly apparent, wavelet transforms can also be used in the development and, potentially, final deployment of automated algorithms for volcano-seismic analysis. The ability to suitably represent co-occurring signals across many orders of scale, conduct more complex filtering through phase attributes, and adjust template functions (i.e., mother wavelets) to suit the purpose of the study, make the CWT an extremely versatile tool for event classification and interpretation of physical source mechanisms.

The 'edge detection' capabilities of the CWT also reveal sharp changes in signal, which can be used in conjunction with the broadband seismometer's sensitivity to rotational motion to characterise deformation dynamics at volcanic systems and identify explosion events. Drawbacks include low time resolution at very low frequencies – as such, CWT analysis may prove most useful during exploratory stages of analysis, identifying where very low frequency events occur, characterising their main spectral peaks and relating them to coincident finer-scale processes, before employing causal filters across frequency bands of interest to better constrain onset, duration and characteristic waveform.

The high temporal resolution of less oscillatory wavelets (e.g., Haar wavelet or Morlet wavelet with low central frequency) also enhance identification of first breaks and characterisation of transient event durations, both of which aid event picking and classification, as well as provide

good approximations of the first- and second-order signal derivatives. Finally, the CWT's corresponding distribution of wavelet energy can be used to generate weighting functions from sections of seismic noise to improve signal-to-noise ratios in subsequent scalograms, or even the signal itself. Although not used in this paper, other wavelet templates may provide better fidelity to particular signal features of interest, yielding greater T-F localisation and discrimination.

ACKNOWLEDGEMENTS

The facilities of IRIS Data Services, and specifically the IRIS Data Management Center, were used for access to some of the waveforms and related metadata used in this study. IRIS Data Services are funded through the Seismological Facilities for the Advancement of Geoscience and EarthScope (SAGE) Proposal of the National Science Foundation under Cooperative Agreement EAR-1261681.

WoVI was funded by NSF grant EAR-1530804 to Jeff Johnson, the Smithsonian Institution, and Boise State University. Author SL is supported by a NERC GW4+ Doctoral Training Partnership studentship from the Natural Environment Research Council [NE/L002434/1]. Author SDA is supported by NERC grants NE/P007708/1 and NE/P00105X/1, and author KVC is supported by the AXA Research Fund and a Royal Society Wolfson Merit Award.

We are grateful for the constructive input of two anonymous reviewers whose suggestions helped improve this manuscript.

REFERENCES

Addison, P.S., 2018. Introduction to redundancy rules: the continuous wavelet transform comes of age. Philos. Trans. R. Soc. A Math. Phys. Eng. Sci. 376. https://doi.org/10.1098/rsta.2017.0258

Addison, P.S., 2016. The Illustrated Wavelet Transform Handbook : Introductory Theory and Applications in Science, Engineering, Medicine and Finance, Second Edition. ed. CRC Press, Boca Raton, FL.

Addison, P.S., Watson, J.N., Feng, T., 2002. Low-oscillation complex wavelets. J. Sound Vib. 254, 733–762. https://doi.org/10.1006/jsvi.2001.4119

Aguiar-Conraria, L., Soares, M.J., 2011. The Continuous Wavelet Transform: A Primer. NIPE Working Paper., Núcleo de Investigação em Políticas Económicas, Universidade Do Minho.

Anderson, J.F., Lees, J.M., Waite, G.P., Johnson, J.B., 2012. Source and propagation effects on Near-Field co-eruptive ground motion at Santiaguito volcano, Guatemala. Bull. Seismol. Soc. Am. 102, 696–706. https://doi.org/10.1785/0120110106

Aoyama, H., Oshima, H., 2008. Tilt change recorded by broadband seismometer prior to small phreatic explosion of Meakan-dake volcano, Hokkaido, Japan. Geophys. Res. Lett. 35, 1–7. https://doi.org/10.1029/2007GL032988

Aster, R., Zandomeneghi, D., Mah, S., McNamara, S., Henderson, D.B., Knox, H., Jones, K., 2008. Moment tensor inversion of very long period seismic signals from Strombolian eruptions of Erebus Volcano. J. Volcanol. Geotherm. Res. 177, 635–647. https://doi.org/10.1016/J.JVOLGEORES.2008.08.013

Bartosch, T., Seidl, D., 1999. Spectrogram analysis of selected tremor signals using short-time Fourier transform and continuous wavelet transform. Ann. Geophys. https://doi.org/10.4401/ag-3733

Bean, C.J., De Barros, L., Lokmer, I., Métaxian, J.-P., O' Brien, G., Murphy, S., 2013. Long-period seismicity in the shallow volcanic edifice formed from slow-rupture earthquakes. Nat. Geosci. 7, 71–75. https://doi.org/10.1038/ngeo2027

Bicego, M., Acosta-Munoz, C., Orozco-Alzate, M., 2013. Classification of seismic volcanic signals using hidden-markov-model-based generative embeddings. IEEE Trans. Geosci. Remote Sens. 51, 3400–3409. https://doi.org/10.1109/TGRS.2012.2220370

Bluth, G.J.S., Rose, W.I., 2004. Observations of eruptive activity at Santiaguito volcano, Guatemala. J. Volcanol. Geotherm. Res. 136, 297–302. https://doi.org/10.1016/j.jvolgeores.2004.06.001

Bogiatzis, P., Ishii, M., 2015. Continuous Wavelet Decomposition Algorithms for Automatic Detection of Compressional- and Shear-Wave Arrival Times. Bull. Seismol. Soc. Am. 105, 1628–1641. https://doi.org/10.1785/0120140267

Bowman, D.C., Lees, J.M., 2013. The Hilbert–Huang Transform: A High Resolution Spectral Method for Nonlinear and Nonstationary Time Series. Seismol. Res. Lett. 84, 1074–1080. https://doi.org/10.1785/0220130025

Bromirski, P.D., Stephen, R.A., Gerstoft, P., 2013. Are deep-ocean-generated surface-wave microseisms observed on land? J. Geophys. Res. Solid Earth 118, 3610–3629. https://doi.org/10.1002/jgrb.50268

Cannata, A., Cannavò, F., Montalto, P., Ercoli, M., Mancinelli, P., Pauselli, C., Leto, G., 2017. Monitoring crustal changes at volcanoes by seismic noise interferometry: Mt. Etna case of study. J. Volcanol. Geotherm. Res. 337, 165–174. https://doi.org/10.1016/j.jvolgeores.2017.03.023

Cannata, A., Montalto, P., Patanè, D., 2013. Joint analysis of infrasound and seismic signals by cross wavelet transform: Detection of Mt. Etna explosive activity. Nat. Hazards Earth Syst. Sci. 13, 1669–1677. https://doi.org/10.5194/nhess-13-1669-2013

Chakraborty, A., Okaya, D., 1995. Frequency-time decomposition of seismic data using wavelet-based methods. GEOPHYSICS 60, 1906–1916. https://doi.org/10.1190/1.1443922

Chouet, B., Dawson, P., Arciniega-Ceballos, A., 2005. Source mechanism of Vulcanian degassing at Popocatépetl Volcano, Mexico, determined from waveform inversions of very long period signals. J. Geophys. Res. Solid Earth 110, B07301. https://doi.org/10.1029/2004JB003524

Chouet, B., Dawson, P., Martini, M., 2008. Shallow-conduit dynamics at Stromboli Volcano, Italy, imaged from waveform inversions. Geol. Soc. London, Spec. Publ. 307, 57–84. https://doi.org/10.1144/SP307.5

Chouet, B.A., Dawson, P.B., James, M.R., Lane, S.J., 2010. Seismic source mechanism of degassing bursts at Kilauea Volcano, Hawaii: Results from waveform inversion in the 10-50 s band. J. Geophys. Res. Solid Earth 115, 1–24. https://doi.org/10.1029/2009JB006661

Chouet, B.A., Matoza, R.S., 2013. A multi-decadal view of seismic methods for detecting precursors of magma movement and eruption. J. Volcanol. Geotherm. Res. 252, 108–175. https://doi.org/10.1016/j.jvolgeores.2012.11.013

Conde, V., Bredemeyer, S., Saballos, J.A., Galle, B., Hansteen, T.H., 2016. Linking SO2 emission rates and seismicity by continuous

wavelet transform: implications for volcanic surveillance at San Cristóbal volcano, Nicaragua. Int. J. Earth Sci. 105, 1453–1465. https://doi.org/10.1007/s00531-015-1264-1

Cooley, J.W., Tukey, J.W., 1965. An Algorithm for the Machine Calculation of Complex Fourier Series. Math. Comput. 19, 297–301.

Curilem, M., Huenupan, F., Beltrán, D., San Martin, C., Fuentealba, G., Franco, L., Cardona, C., Acuña, G., Chacón, M., Khan, M.S., Becerra Yoma, N., 2016. Pattern recognition applied to seismic signals of Llaima volcano (Chile): An evaluation of station-dependent classifiers. J. Volcanol. Geotherm. Res. 315, 15–27. https://doi.org/10.1016/j.jvolgeores.2016.02.006

D'Auria, L., Giudicepietro, F., Martini, M., Peluso, R., 2006. Seismological insight into the kinematics of the 5 April 2003 vulcanian explosion at Stromboli volcano (southern Italy). Geophys. Res. Lett. 33, 10–13. https://doi.org/10.1029/2006GL026018

Daubechies, I., 1992. Ten Lectures on Wavelets. Society for Industrial and Applied Mathematics. https://doi.org/10.1137/1.9781611970104

De Angelis, S., Lamb, O.D., Lamur, A., Hornby, A.J., von Aulock, F.W., Chigna, G., Lavallée, Y., Rietbrock, A., 2016. Characterization of moderate ash-and-gas explosions at Santiaguito volcano, Guatemala, from infrasound waveform inversion and thermal infrared measurements. Geophys. Res. Lett. 43, 6220–6227. https://doi.org/10.1002/2016GL069098

Delorey, A.A., Vidale, J., Steim, J., Bodin, P., 2008. Broadband Sensor Nonlinearity during Moderate Shaking. Bull. Seismol. Soc. Am. 98, 1595–1601. https://doi.org/10.1785/0120070225

Genco, R., Ripepe, M., 2010. Inflation-deflation cycles revealed by tilt and seismic records at Stromboli volcano. Geophys. Res. Lett. 37, 1–5. https://doi.org/10.1029/2010GL042925

Goldstein, P., Snoke, A., 2005. SAC Availability for the IRIS Community. Inc. Institutions Seismol. Data Manag. Cent. Electron. Newsl.

Goupillaud, P., Grossmann, A., Morlet, J., 1984. Cycle-octave and related transforms in seismic signal analysis. Geoexploration 23, 85–102. https://doi.org/10.1016/0016-7142(84)90025-5

Grossmann, A., Morlet, J., 1984. Decomposition of Hardy Functions Into. SIAM J. Math. Anal. 15.

Haney, M.M., Power, J., West, M., Michaels, P., 2012. Causal Instrument Corrections for Short-Period and Broadband Seismometers. Seismol. Res. Lett. 83, 834–845. https://doi.org/10.1785/0220120031

Harris, A.J.L., Rose, W.I., Flynn, L.P., 2003. Temporal trends in lava dome extrusion at Santiaguito 1922-2000. Bull. Volcanol. 65, 77–89. https://doi.org/10.1007/s00445-002-0243-0

Hibert, C., Mangeney, A., Grandjean, G., Shapiro, N.M., 2011. Slope instabilities in Dolomieu crater, Réunion Island: From seismic signals to rockfall characteristics. J. Geophys. Res. Earth Surf. 116, 1–18. https://doi.org/10.1029/2011JF002038

Hibert, C., Provost, F., Malet, J.P., Maggi, A., Stumpf, A., Ferrazzini, V., 2017. Automatic identification of rockfalls and volcano-tectonic earthquakes at the Piton de la Fournaise volcano using a Random Forest algorithm. J. Volcanol. Geotherm. Res. 340, 130–142. https://doi.org/10.1016/j.jvolgeores.2017.04.015

Hill, D.P., Dawson, P., Johnston, M.J.S., Pitt, A.M., Biasi, G., Smith, K., 2002. Very-long-period volcanic earthquakes beneath Mammoth Mountain, California. Geophys. Res. Lett. 29, 8-1-8–4. https://doi.org/10.1029/2002GL014833

Holland, A.S.P., Watson, I.M., Phillips, J.C., Caricchi, L., Dalton, M.P., 2011. Degassing processes during lava dome growth: Insights from Santiaguito lava dome, Guatemala. J. Volcanol. Geotherm. Res. 202, 153–166. https://doi.org/10.1016/j.jvolgeores.2011.02.004

Johnson, J.B., Lyons, J.J., Andrews, B.J., Lees, J.M., 2014. Explosive dome eruptions modulated by periodic gas-driven inflation. Geophys. Res. Lett. 41, 6689–6697. https://doi.org/10.1002/2014GL061310

Johnson, J.B., Sanderson, R., Lyons, J., Escobar-Wolf, R., Waite, G., Lees, J.M., 2009. Dissection of a composite volcanic earthquake at Santiaguito, Guatemala. Geophys. Res. Lett. 36, 1–5. https://doi.org/10.1029/2009GL039370

Johnson, J.B., Watson, L.M., Palma, J.L., Dunham, E.M., Anderson, J.F., 2018. Forecasting the Eruption of an Open-Vent Volcano Using Resonant Infrasound Tones. Geophys. Res. Lett. 45, 2213–2220. https://doi.org/10.1002/2017GL076506

Karamzadeh, N., Doloei, G.J., Reza, A.M., 2013. Automatic earthquake signal onset picking based on the continuous wavelet transform. IEEE Trans. Geosci. Remote Sens. 51, 2666–2674. https://doi.org/10.1109/TGRS.2012.2213824

Kawakatsu, H., Kaneshima, S., Matsubayashi, H., Ohminato, T., Sudo, Y., Tsutsui, T., Uhira, K., Yamasato, H., Ito, H., Legrand, D., 2000. Aso94: Aso seismic observation with broadband instruments. J. Volcanol. Geotherm. Res. 101, 129–154. https://doi.org/10.1016/S0377-0273(00)00166-9

Koper, K.D., Burlacu, R., 2015. The fine structure of souble-frecuency microseisms recorded by seismometers in North America. J. Geophys. Res. Solid Earth 120, 1677–1691. https://doi.org/10.1002/2014JB011820.Received

Kulesh, M., Diallo, M.S., Holschneider, M., Kurennaya, K., Krüger, F., Ohrnberger, M., Scherbaum, F., 2007. Polarization analysis in the wavelet domain based on the adaptive covariance method. Geophys. J. Int. 170, 667–678. https://doi.org/10.1111/j.1365-246X.2007.03417.x

Lahr, J.C., Chouet, B.A., Stephens, C.D., Power, J.A., Page, R.A., 1994. Earthquake classification, location, and error analysis in a volcanic

environment: implications for the magmatic system of the 1989–1990 eruptions at redoubt volcano, Alaska. J. Volcanol. Geotherm. Res. 62, 137–151. https://doi.org/10.1016/0377-0273(94)90031-0

Lees, J.M., Ruiz, M., 2008. Non-linear explosion tremor at Sangay, Volcano, Ecuador. J. Volcanol. Geotherm. Res. 176, 170–178. https://doi.org/10.1016/j.jvolgeores.2007.08.012

Liu, Y., Liang, X.S., Weisberg, R.H., 2007. Rectification of the bias in the wavelet power spectrum. J. Atmos. Ocean. Technol. 24, 2093–2102. https://doi.org/10.1175/2007JTECHO511.1

Lu, Z., Wicks, C., Power, J.A., Dzurisin, D., 2000. Ground deformation associated with the March 1996 earthquake swarm at Akutan volcano, Alaska, revealed by satellite radar interferometry. J. Geophys. Res. Earth 105, 21483–21495. https://doi.org/10.1029/2000JB900200

Lyons, J.J., Waite, G.P., 2011. Dynamics of explosive volcanism at Fuego volcano imaged with very long period seismicity. J. Geophys. Res. Solid Earth 116, 1–18. https://doi.org/10.1029/2011JB008521

Lyons, J.J., Waite, G.P., Ichihara, M., Lees, J.M., 2012. Tilt prior to explosions and the effect of topography on ultra-long-period seismic records at Fuego volcano, Guatemala. Geophys. Res. Lett. 39, 1–6. https://doi.org/10.1029/2012GL051184

Maggi, A., Ferrazzini, V., Hibert, C., Beauducel, F., Boissier, P., Amemoutou, A., 2017. Implementation of a Multistation Approach for Automated Event Classification at Piton de la Fournaise Volcano. Seismol. Res. Lett. 88, 878–891. https://doi.org/10.1785/0220160189

Mallat, S., 2009. A Wavelet Tour of Signal Processing, 3rd editio. ed. Elsevier. https://doi.org/10.1016/B978-0-12-374370-1.X0001-8

McCausland, W.A., Gunawan, H., White, R.A., Indrastuti, N., Patria, C., Suparman, Y., Putra, A., Triastuty, H., Hendrasto, M., 2017. Using a process-based model of pre-eruptive seismic patterns to forecast evolving eruptive styles at Sinabung Volcano, Indonesia. J. Volcanol. Geotherm. Res. xxx, xxx-xxx (In Press, Corrected Proof). https://doi.org/10.1016/j.jvolgeores.2017.04.004

McKee, K., Iezzi, A., Roman, D., Fee, D., Johnson, J., 2015. Workshops on Volcanoes 2016, Santiaguito, Guatemala. https://doi.org/10.7914/SN/1F_2015

McNutt, S.R., 1996. Seismic Monitoring and Eruption Forecasting of Volcanoes: A Review of the State-of-the-Art and Case Histories, in: Monitoring and Mitigation of Volcano Hazards. Springer Berlin Heidelberg, Berlin, Heidelberg, pp. 99–146. https://doi.org/10.1007/978-3-642-80087-0_3

McNutt, S.R., Roman, D.C., 2015. Volcanic Seismicity. Encycl. Volcanoes. https://doi.org/10.1016/B978-0-12-385938-9.00059-6

Meyers, S.D., Kelly, B.G., O'Brien, J.J., 1993. An Introduction to Wavelet Analysis in Oceanography and Meteorology: With Application to the Dispersion of Yanai Waves. Mon. Weather Rev. 121, 2858–2866. https://doi.org/10.1175/1520-0493(1993)121<2858:aitwai>2.0.co;2

Moran, S.C., Newhall, C., Roman, D.C., 2011. Failed magmatic eruptions: Late-stage cessation of magma ascent. Bull. Volcanol. 73, 115–122. https://doi.org/10.1007/s00445-010-0444-x

Morlet, J., Arens, G., Fourgeau, E., Giard, D., 1982a. Wave propagation and sampling theory—Part II: Sampling theory and complex waves. Geophysics 47, 222–236. https://doi.org/10.1190/1.1441329

Morlet, J., Arens, G., Fourgeau, E., Glard, D., 1982b. Wave propagation and sampling theory—Part I: Complex signal and scattering in multilayered media. Geophysics 47, 203–221. https://doi.org/10.1190/1.1441328

Nie, L., Wu, S., Lin, X., Zheng, L., Rui, L., 2002. Approximate derivative calculated by using continuous wavelet transform. J. Chem. Inf. Comput. Sci. 42, 274–283. https://doi.org/10.1021/ci010333v

Odbert, H.M., Stewart, R.C., Wadge, G., 2014. Chapter 2 Cyclic phenomena at the Soufriere Hills Volcano, Montserrat. Geol. Soc. London, Mem. 39, 41–60. https://doi.org/10.1144/M39.2

Percival, D.P., 1995. On Estimation of the Wavelet Variance. Biometrika 82, 619–631. https://doi.org/10.2307/2337538

Phillipson, G., Sobradelo, R., Gottsmann, J., 2013. Global volcanic unrest in the 21st century: An analysis of the first decade. J. Volcanol. Geotherm. Res. 264, 183–196. https://doi.org/10.1016/J.JVOLGEORES.2013.08.004

Power, J.A., Jolly, A.D., Page, R.A., McNutt, S.R., 1992. Seismicity and Forecasting of the 1992 Eruptions of Crater Peak Vent , Mount Spurr Volcano , Alaska : An Overview.

R Core Team, 2017. R: A Language and Environment for Statistical Computing.

Roman, D.C., Neuberg, J., Luckett, R.R., 2006. Assessing the likelihood of volcanic eruption through analysis of volcanotectonic earthquake fault–plane solutions. Earth Planet. Sci. Lett. 248, 244–252. https://doi.org/10.1016/j.epsl.2006.05.029

Roman, D.C., Power, J.A., 2011. Mechanism of the 1996-97 non-eruptive volcano-tectonic earthquake swarm at Iliamna Volcano, Alaska. Bull. Volcanol. 73, 143–153. https://doi.org/10.1007/s00445-010-0439-7

Roman, D.C., Power, J.A., Moran, S.C., Cashman, K. V, Doukas, M.P., Neal, C.A., Gerlach, T.M., 2004. Evidence for dike emplacement

beneath Iliamna Volcano, Alaska in 1996. J. Volcanol. Geotherm. Res. 130, 265–284. https://doi.org/10.1016/S0377-0273(03)00302-0

Rose, W.I., 1972. Notes on the 1902 eruption of Santa María volcano, Guatemala. Bull. Volcanol. 36, 29–45. https://doi.org/10.1007/BF02596981

Sanderson, R.W., Johnson, J.B., Lees, J.M., 2010. Ultra-long period seismic signals and cyclic deflation coincident with eruptions at Santiaguito volcano, Guatemala. J. Volcanol. Geotherm. Res. 198, 35–44. https://doi.org/10.1016/j.jvolgeores.2010.08.007

Saracco, G., Labazuy, P., Moreau, F., 2004. Localization of self-potential sources in volcano-electric effect with complex continuous wavelet transform and electrical tomography methods for an active volcano. Geophys. Res. Lett. 31, 1–5. https://doi.org/10.1029/2004GL019554

Schukin, E.L., Zamaraev, R.U., Schukin, L.I., 2004. The optimisation of wavelet transform for the impulse analysis in vibration signals. Mech. Syst. Signal Process. 18, 1315–1333. https://doi.org/10.1016/j.ymssp.2004.01.008

Shao, X., Ma, C., 2003. A general approach to derivative calculation using wavelet transform. Chemom. Intell. Lab. Syst. 69, 157–165. https://doi.org/10.1016/j.chemolab.2003.08.001

Shirzaei, M., 2013. A wavelet-based multitemporal DInSAR algorithm for monitoring ground surface motion. IEEE Geosci. Remote Sens. Lett. 10, 456–460. https://doi.org/10.1109/LGRS.2012.2208935

Soubestre, J., Shapiro, N.M., Seydoux, L., Rosny, J. De, Droznin, D. V, Droznina, S.Y., Senyukov, S.L., Gordeev, E.I., 2018. Journal of Geophysical Research : Solid Earth Network-Based Detection and Classification of Seismovolcanic Tremors : Example From the Klyuchevskoy Volcanic Group in Kamchatka. https://doi.org/10.1002/2017JB014726

Tary, J.B., Herrera, R.H., Han, J., Baan, M. Van Der, 2014. Reviews of Geophysics Spectral estimation — What is new? What is next? Rev. Geophys. 52, 723–749. https://doi.org/10.1002/2014RG000461

Tary, J.B., Herrera, R.H., van der Baan, M., 2018. Analysis of time-varying signals using continuous wavelet and synchrosqueezed transforms. Philos. Trans. R. Soc. A Math. Phys. Eng. Sci. 376. https://doi.org/10.1098/rsta.2017.0254

Torrence, C., Compo, G.P., 1998. A practical guide to wavelet analysis. Bull. Am. Meteor. Soc. 79, 61–78. https://doi.org/10.1175/1520-0477(1998)079<0061:APGTWA>2.0.CO;2

Vargas-Bracamontes, D.M., Nava, F.A., Reyes-Dávila, G.A., 2009. Time-scale wavelet patterns related to the 1998–1999 eruptions of the Colima volcano, and their possible implications for eruption forecasting. J. Volcanol. Geotherm. Res. 184, 271–284. https://doi.org/10.1016/j.jvolgeores.2009.01.025

Waite, G.P., Nadeau, P.A., Lyons, J.J., 2013. Variability in eruption style and associated very long period events at Fuego volcano, Guatemala. J. Geophys. Res. Solid Earth 118, 1526–1533. https://doi.org/10.1002/jgrb.50075

White, R., McCausland, W., 2016. Volcano-tectonic earthquakes: A new tool for estimating intrusive volumes and forecasting eruptions. J. Volcanol. Geotherm. Res. 309, 139–155. https://doi.org/10.1016/j.jvolgeores.2015.10.020

Wielandt, E., Forbriger, T., 1999. Near-field seismic displacement and tilt associated with the explosive activity of Stromboli. Ann. Geophys. https://doi.org/10.4401/ag-3723

Wiens, D.A., Pozgay, S.H., Shore, P.J., Sauter, A.W., White, R.A., 2005. Tilt recorded by a portable broadband seismograph: The 2003 eruption of Anatahan Volcano, Mariana Islands. Geophys. Res. Lett. 32, 1–4. https://doi.org/10.1029/2005GL023369

Williams, S.N., Self, S., 1983. The October 1902 plinian eruption of Santa Maria volcano, Guatemala. J. Volcanol. Geotherm. Res. 16, 33–56. https://doi.org/10.1016/0377-0273(83)90083-5

APPENDIX 1 – R CODE FOR CWT USING MORLET WAVELET

```
MorletCWT <- function(x, dt, dj, lp, up, omega0=6) {

      # x = signal
      # dt = sample rate (delta)
      # dj = no. of voices per octave (no. of sub-scales)
      # lp = lower period ( 1/frequency )
      # up = upper period ( 1/frequency )
      # omega0 = central frequency of Morlet wavelet

    # Original length of signal and length of zero padding:
    series.length <- length(x)
    N <- 2^ceiling(log2(series.length)) # Next dyadic value
    pad.length <- N-series.length

    # Conversion to Fourier freq
    f0 = (2*pi)/omega0

    # Convert lower and upper periods to minimum and maximum wavelet scale
    min.scale <- lp/f0
    max.scale <- up/f0
    min.scale.index <- ceiling(log2(min.scale)/dj)*dj
    max.scale.index <- floor(log2(max.scale)/dj)*dj

    # Create sequence of wavelet scales
    scales <- 2^seq(from=min.scale.index, to=max.scale.index, by=dj)
    scales.length <- length(scales)

    # Sequence of periods (for plotting)
    periods <- f0*scales

    # Computation of angular frequencies - from Torrence & Compo 1998
    omega.k.part1 <- 0:(N/2)
    omega.k.part1 <- (omega.k.part1*2*pi)/(N*dt)
    omega.k.part2 <- ((N/2)+1):(N-1)
    omega.k.part2 <- -(omega.k.part2*2*pi)/(N*dt)
    omega.k <- c(omega.k.part1, omega.k.part2)

    # Standardise x and pad with zeros
    x <- (x-mean(x))/sd(x)
    xpad <- c(x, rep(0,pad.length))

    # Compute FFT of xpad
    fft.xpad <- fft(xpad)

    # Prepare a complex matrix to accommodate wavelet transform
    wave <- matrix(0, nrow=scales.length, ncol=N)
    wave <- wave + 1i*wave

    # Computation for each wavelet scale
    for (i in (1:scales.length)) {

        my.scale <- scales[i]
```

```
        # Normalisation factor
        norm.factor <- pi^(1/4) * sqrt(2*my.scale/dt)

        # FT of wavelet
        expnt.1 <- -( (my.scale * omega.k - omega0)^2 / 2 )
        expnt.2 <- -( ((my.scale * omega.k)^2 + omega0^2) / 2 ) # Non-zero mean correction
        daughter <- norm.factor * (exp(expnt.1) - exp(expnt.2))

        daughter <- daughter * (as.numeric(omega.k > 0)) # Heaviside step function from T&C 1998

        # Calculate CWT via inverse FFT
        wave[i,] <- fft( fft.xpad * daughter, inverse=TRUE) / N
    }

    # Cut out the wavelet transform from padded signal
    output <- list(wave = wave[,1:series.length], f=1/periods, t=seq(from=dt, to=length(x)*dt, by=dt))
    return(output)

}
```